Chapter 2

Critical discussion of spectroscopic diagnostic techniques and their application to CDS data

CDS was designed with sufficient spectral resolution to enable EUV spectroscopic diagnostic techniques in determining coronal plasma parameters (density, temperature and abundance). In this chapter, the main diagnostic methods are described and compared, explaining the choice of techniques employed in this thesis.

The adopted methods and the software that was developed are described, with details of the recommended techniques and line selection for use with CDS. All the comments are based on the experience gained during the last three years from the analysis of a large number of CDS spectra and from comparisons with spectral data from other instruments in the same wavelength range, mainly the Skylab data and high-resolution SERTS data. Here only a summary of the main diagnostics that were found to be more appropriate for use with CDS are presented. A description of CDS, and the full CDS line identification and comparison of observations with theoretical calculations are given in Chapter 3. Examples of spectra and the assessment of line blending is also given in Chapter 3.

The main density and temperature diagnostics based on line ratio techniques are presented in Sections 2.1 to 2.3, while Section 2.4 describes the method developed to derive the differential emission measure (DEM).

Section 2.5 focuses on a critical discussion of emission measure (and differential emission measure) techniques and the evaluation of element abundances. This is based on a re-analysis of the Skylab coronal hole spectral data. Various concepts and definitions that will be used in the remainder of this thesis are also explained here. Some interesting results of this re-analysis are presented, revealing departures from previous results which casts some doubt on the applicability of ionization equilibrium for ions of the Li-like sequence.

Section 2.6 contains a critical discussion (with examples and a re-analysis of Skylab data) of previous work on element abundances, showing how various effects can change the results, in particular showing the importance of the inclusion of the thermal distribution along the line of sight (the DEM) in the calculations for the element abundances, something that has been neglected in the past in most cases. A discussion of the potential of CDS spectra for element abundance analysis is also presented.

2.1 Electron density diagnostics

CDS observations can be used to estimate average electron densities along the line of sight, using density-sensitive ratios of lines emitted from the same ion.

Theoretical calculations for EUV lines, useful for coronal hole and quiet region density diagnostics, have been presented, in some cases together with comparisons with observations, by a large number of authors. Also many review papers have been written on the subject. A useful long bibliography of spectroscopic diagnostics in the EUV-UV, organised by isoelectronic sequence, is given by *Keenan* (1996). Some of the most useful publications about density diagnostics in the CDS wavelength range are now briefly mentioned. *Dwivedi and Raju* (1980) present density diagnostics for Mg VIII and Si X lines. *Mason and Monsignori Fossi* (1994) present a review paper on spectroscopic diagnostics for solar and stellar plasma. *Masai* (1994) studied O V (and Fe XXII) density diagnostics for application to tokamak plasma, pointing out the diagnostic capabilities for these ions. *Keenan et al.* (1994) present O V diagnostics applied to solar observations. *Dwivedi and Mohan* (1995a) present Mg VIII calculations applied to coronal hole Skylab observations. *Dwivedi and Mohan* (1995c) present Ne V and Mg V diagnostics with solar applications. *Foster et al.* (1997) analyse various Mg VIII line ratios and compare them with Skylab observations; *Mason et al.* (1997) apply spectroscopic diagnostics to CDS observations for the first time. Finally, many papers have been written on applications of the SERTS-89 observations presented by *Thomas and Neupert* (1994). For example, *Brickhouse et al.* (1995) have presented an analysis of the Fe ions, including density diagnostics, while *Del Zanna et al.* (1995) have previously produced a more complete differential emission measure analysis using many ions of different elements. *Young et al.* (1998) have recently presented a complete analysis, including recalibration, of the SERTS-89 spectrum, with a description of the density diagnostics used. *Dwivedi et al.* (1998) have also presented a list of diagnostics to be applied to the SERTS-89 spectrum.

A large effort was spent in checking which of the many proposed diagnostics were applicable to CDS, or if there were new ones not proposed by previous authors, in order to select the most useful ones. A set of CHIANTI routines that calculate the level populations and present the ratio of lines of the same ion, calculated at constant temperature, have been used for this purpose. In the majority of cases, the CHIANTI calculations were found to be in agreement with the other calculations found in the literature. A set of IDL routines were written by the author to convert the observed ratio values with their errors to density values, performing spline interpolation between the theoretical points. Although a full critical description of the various density diagnostics is beyond the scope of this Chapter, there are some key points that are worth considering.

1. It has to be noted that all the density diagnostics used in this thesis calculate the line ratios at the temperature of maximum ionization fraction, and some degree of approximation is therefore introduced. Figure 2.1 shows the density-sensitive Si IX ratio calculated at three temperatures ($T = 10^6$ K is the temperature of maximum ionization fraction for Si IX), showing that these temperature variations do not appreciably affect the ratio.

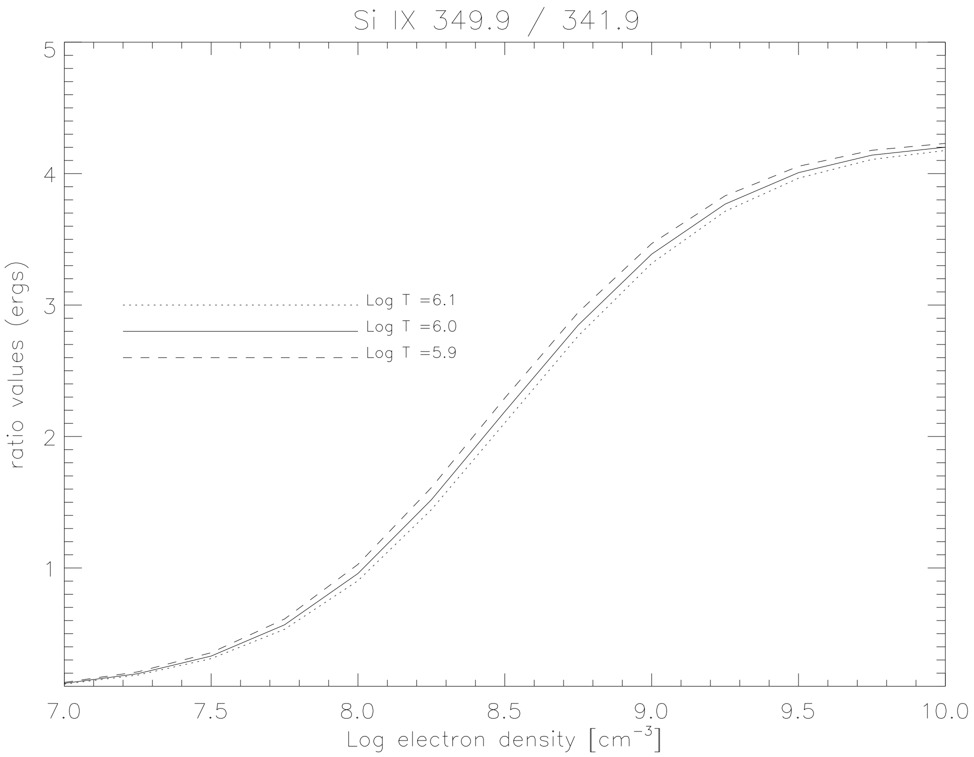

Figure 2.1: *The density-sensitive Si IX ratio and its variation with temperature.*

2. The process of photoionization, that is not included in the CHIANTI routines, can have some effects on the density estimation. The radiation that comes from the solar photosphere can excite transitions between levels in the ground configuration of ions in the corona, mainly affecting the level balance calculations for very low densities

($N_e \leq 10^8$ cm^{-3}, see *Young*, 1998t). The effect is stronger close to the photosphere, and tends to die out with height because of the decrease of the photospheric radiation field with distance. This decrease can be accounted for by estimating a geometric dilution factor that is a function of height above the photosphere. Si IX should be affected more than other ions.

Photoionization has not been taken into account in this thesis, partly because of the difficulty in estimating the height of the emitting plasma for on-disc observations, where all the plasma at all heights in principle contributes to the observed emission. The introduction of the photoionization would have the effect of lowering the electron densities derived from the observations (possibly by up to 30-40% for Si IX), so the densities derived from Si IX in this thesis should be treated as upper values, in cases when $N_e \leq 10^8$ cm^{-3}. A possible estimate of the real importance of the photoionization process for this issue can be given comparing densities obtained by transitions that can be affected with those that are not, in off-limb observations. It should be noted that no obvious effects due to photoionization were found in the spectra analysed, if we except a coronal hole off-limb observation (see Section 6.2).

3. Many density diagnostics proposed in the literature involve ratios of lines emitted by different elements (*Dwivedi and Mohan*, 1995b; *Dwivedi and Mohan*, 1995c). In view of the fact that small differences in contribution functions can be very important indeed, and in view of the uncertainties of the elemental abundance evaluations, it was felt that these diagnostics should *not* be used.

4. As already mentioned, the various line ratios usually produce a large scatter of values, and it is therefore important to confirm any density estimate with other estimates based on the maximum possible number of different line ratios. Also, there are some well known density ratios that produce results which strongly disagree with those derived from ions that are emitted at similar temperatures.

5. Most of the observed diagnostic lines are very weak, which makes the data analysis difficult.

6. Then last, but not least, is the fact that many proposed diagnostic ratios are affected by blending which varies depending on the type of source observed, and which is particularly strong at the moderate resolution of CDS.

Table 2.1 presents a list of useful line ratios available with CDS, while Figure 2.2 shows how some of these ratios vary with density. Only the principal usable ratios are listed, involving pairs of lines seen by the same spectrometer and detector. In fact, the use of pairs seen by different spectrometers is severely limited by any time variability of the

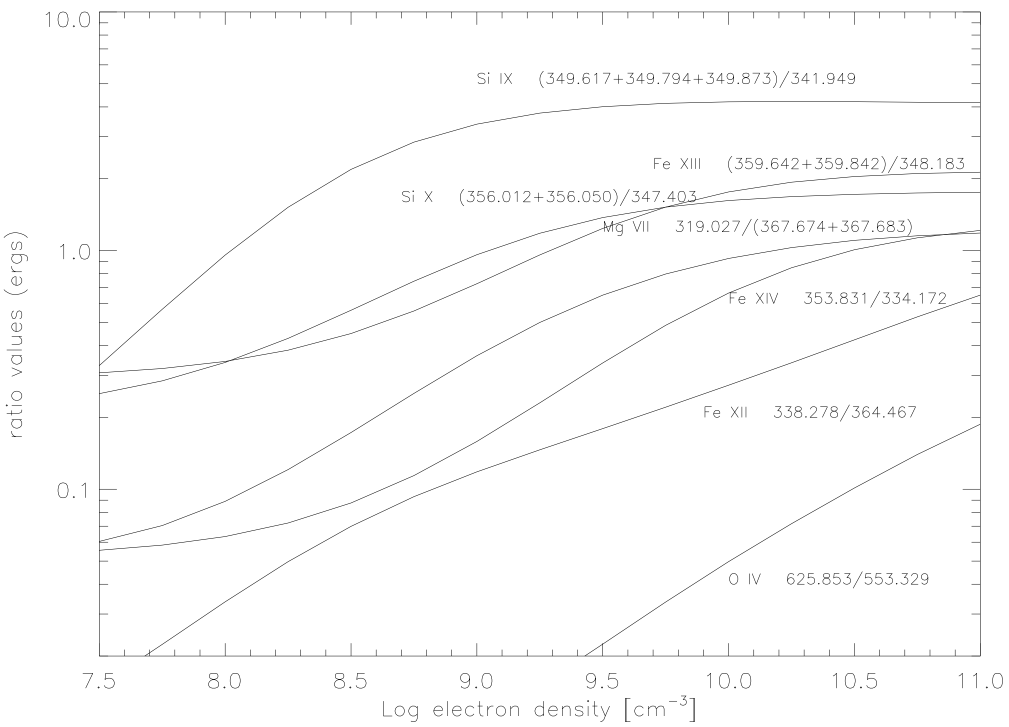

Figure 2.2: *Some useful density-sensitive line ratios observed by CDS.*

Table 2.1: *Density sensitive line ratios observed by CDS, ordered by the temperature of maximum of the contribution functions shown in column 4, calculated with the ionization equilibrium calculations of* Arnaud and Rothenflug *(1985). The ranges for which the ratios can be used are shown in column 5. The numbers in parentheses indicate the number of transitions that compose the self-blends. The lines indicated with a (!) have problems in either their observation or in the atomic physics. The lines indicated with a (*) are the best selection within a wider choice. The detectors in parentheses indicate that the lines are also visible in second order. N means NIS, and G means GIS; the NIS and GIS channels are described in Chapter 3.*

Ion	Ratio (Å)	Detector	log T_{max}	log N_e
O IV	625.853 (!) / 608.397 (*)	N 2	5.27	8.0 – 11.0
Mg VII	319.027 (!) / 367.7 (2) (*)	N 1	5.81	7.0 – 10.0
Mg VII	280.737 / 434.700 (*)	G 3	5.81	7.0 – 10.0
Mg VIII	315.038 / 317.038	N 1	5.91	7.0 – 8.5
Mg VIII	315.038 / 313.754	N 1	5.91	7.0 – 8.5
Mg VIII	436.7 (2) / 430.465	G 3	5.91	7.0 – 9.0
Si IX	349.9 (3) / 341.949	N 1 (G 4)	6.02	7.5 – 9.5
Si IX	345.100 / 341.949	N 1 (G 4)	6.02	7.5 – 9.5
Si IX	349.9 (3) / 345.100	N 1 (G 4)	6.02	7.5 – 9.5
Fe X	175.3 (2) (!) / 174.534 (*)	G 1	6.04	9.0 – 11.0
Fe X	324.763 (!) / 345.722	N 1	6.04	7.0 – 10.0
Si X	356.0 (2) / 347.402	N 1 (G 4)	6.12	8.0 – 10.0
Fe XII	338.278 (!) / 364.467 (!) (*)	N 1 (G 4)	6.16	7.0 – 12.0
Fe XIII	359.6 (2) (!) / 348.18	N 1 (G 4)	6.21	8.5 – 10.5
Fe XIII	320.8 (!) / 348.18	N 1	6.21	7.0 – 10.0
Fe XIII	203.8 (2) / 202.044	G 1	6.21	8.5 – 10.5
Fe XIV	353.83 (!) / 334.17	N 1 (G 4)	6.25	9.0 – 11.0

source and by cross-calibration uncertainties. Many of the ratios are formed between a density-sensitive line and a relatively insensitive one, choosing the brightest and the least affected by blends, which is close in wavelength to the other line (to reduce calibration errors, discussed further in Chapter 3).

The ranges for which the ratios can be used are also shown in Table 2.1, but this does not mean that all the ratios are usable in all cases. Ions like Fe XIII that emit above a million degrees, for example, are simply not seen in coronal holes or in very quiet regions of the Sun. Most of the ratios can be reliable or not depending on the source region observed, because of blending with different lines, either emitted at lower or higher temperatures. The lines indicated with a (!) have problems in either their observation or in the atomic physics. This is based on experience gained in analysing different source regions (e.g. on-disc, off-limb, coronal holes, quiet sun, active regions) with the different detectors, and on the best possible line identification, with DEM analysis of the various regions. Chapter 3 describes some example spectra in detail. Note that most of the reliable density-sensitive ratios are in NIS 1, although in many cases they can be seen in second order in GIS 4.

Comments on the lines in Table 2.1

O IV

The O IV 625.9 Å line is very weak and in the wing of the Mg X 624.9 Å line, but is more visible when the Mg X intensity is reduced, as in coronal holes. This line is density-sensitive and has previously been used in the study of transition region brightenings (*Young and Mason*, 1997). This line could be partly blended with the second order Fe XIII 312.872 Å, but due to the low NIS sensitivity in second order (see Chapter 3), this is only likely to be a problem in active region spectra. The other O IV lines seen in NIS 2 are all strong lines (seen at 553.329, 554.513, 555.263 Å), usually with good agreement between them. O IV 608.4 Å was selected because it is closest to the 625.9 line. Note that an error in the CHIANTI database concerning this, and the line at 609.829 Å, has been discovered and corrected in version 2.

Mg VII

CDS observes many Mg VII lines, of which only two are strongly density-sensitive, at 319.027 and 280.737 Å. The ratio of the 319.027 Å line to any of the three other lines observed in NIS 1, one at 363.772 Å, one at 365.2 Å(self-blend of 365.176 + 365.234 + 365.243 Å), and one at 367.7 Å(self-blend of 367.674 + 367.683 Å) would be a good density diagnostic, but should be used with caution, for many reasons. First, the 319.027 Å is weak (except in plumes or similar low-temperature objects) and can be blended with Ni XV

319.063 Å line, if high-temperature plasma is present along the line of sight . Secondly, the other three lines are very close to other lines, and their measurement is difficult, including the 367.7 Å line, which is the brightest of the three and close to the brightest line of all in the NIS 1 detector, the Mg IX 368 Å line. Thirdly, the 319.027 Å line is quite distant in wavelength from the other lines, and a correct intensity calibration is crucial. The 280.737 Å line is observed in GIS 3. The ratio of this line with any of the relatively bright lines observed in the same detector at 434.7 (434.72 + 434.917), 429.14, 431.2 (431.188 + 431.313) Å is also a good density diagnostic.

Mg VIII

Mg VIII lines are observed in various CDS detectors. The two ratios of the lines visible in NIS 1 are only weakly density-sensitive. The 436.7 (436.735+436.672) Å/ 430.465 Å ratio is one of the best diagnostic ratios that are present in the GIS.

Si IX

CDS observes many Si IX lines, but only those visible in NIS 1 are usable, because those seen in GIS 2 are affected by *ghosts* (see Chapter 3). The lines visible in NIS 1 are seen at 341.949, 345.1, and 349.9 Å. The last is a complex self-blend of three transitions. These lines are free of blends and close in wavelength.

Fe X

The Fe X 175.3 Å line is not strong and lies close to the bright Fe X 174.534 Å so its intensity is not well determined. Its ratio to any of the lines at 174.534, 177.242, 184.543 Å is a good density diagnostic. The Fe X 324.763 Å line is weak and this is the first time it is identified, to the author's knowledge.

Si X

CDS observes many Si X lines, but only the two visible in NIS 1 can be used. They are free from blends and were found to give densities in close agreement with those derived from Si IX. The line at 356.0 Å (a self-blend of two transitions) lies close to other lines, so its intensity must be carefully measured.

Fe XII

Most of the Fe XII lines are observed in NIS 1 and GIS 1. Among them, CHIANTI predicts only a few density-sensitive lines, while all the others have emissivities that vary only slightly with density. Of the three brightest density-sensitive lines, one is seen in GIS 1 at 186.8 Å(a blend of the 186.851 and 186.884 Å lines), while the other two fall in the NIS 1 wavelength range, at 335.339 and 338.278 Å. Unfortunately, the first line at 186.8

Å in normal quiet sun conditions is blended with an Fe VIII 186.6 Å line (Arcetri spectral code), and is therefore not generally usable. In some cases, such as in plumes, where the thermal plasma distribution is biased toward lower temperatures, the Fe VIII 186.6 Å line even becomes dominant.

Only in active region spectra can the contribution from the Fe VIII line be neglected. The derived density is found to be significantly higher than that derived from other ions, as was recently confirmed with high-resolution SERTS observations (*Brosius et al.*, 1998). In their work, the Fe XII ratios 186.8/195.1 and 196.6/193.5 both give much higher densities (log $N_e = 10.0 \pm 0.2$) compared to the densities derived from Fe X, Fe XI, Fe XIII, Fe XIV (log $N_e \simeq 9.4 \pm 0.2$).

Now, considering the lines observed in NIS 1, the 335.339 Å line predicted by CHIANTI has never been identified, since the much stronger Mg VIII 335.253 Å and Fe XVI 335.41 Å lines are too close in wavelength, even for the highest resolution spectrometers. CHIANTI adopts for Fe XII the energy levels of *Jupen et al.* (1993), who present new Fe line identifications based on a detailed comparison of solar, beam-foil, tokamak and laser-produced high-resolution spectra. They reject the identification of the 335.06 Å line, given by *Thomas and Neupert* (1994) (and also found in all the previous literature), and predict an Fe XII line at 335.33 Å. The contribution of this Fe XII line to the observed blend was always assumed to be negligible, probably because most of the EUV spectra analysed were of active regions or obtained during relatively high solar activity, when the Fe XVI 335.41 (the strongest line of the doublet) becomes one of the brightest lines in the whole spectral region. However, our CDS observations indicate that this line *does exist* and gives a non-negligible contribution (as shown in Chapter 3).

In any case, we are left only with the bright Fe XII 338.278 Å line for a density diagnostic. The ratio of the bright Fe XII 338.278 Å with any other Fe XII line observed in NIS 1 would be excellent, as shown in Figure 2.2, since it spans a large density range. The lines that can be used in conjunction with the 338.278 Å line are at 346.852, 352.106 and 364.467 Å. The brightest Fe XII 364.467 Å is partly blended with the Si XI 364.497 Å line, which is only seen in active region spectra, not in coronal holes or the quiet sun. It is possible to estimate the Si XI contribution to the observed line, from the intensities of the other Si XI lines seen in the spectra. The Fe XII 352.106 Å is partly blended with an Al VII 352.149 Å line, while the 346.852 Å line should be free of blends.

However, the ratio of the 338.278 Å line to any of these three lines also gives very high densities at odds with those derived from other ratios. This is not a new result, as it has been observed in many other cases in SERTS spectra (*Brosius et al.*, 1996; *Young et al.*, 1998), but has been explained by the presence of an unidentified line blend. Now, the high spectral resolution of the SERTS spectra (compared to CDS) and also the fact that all the other observed density-sensitive Fe XII lines produce high densities, favours the alternative hypothesis that there is something wrong in the Fe XII theoretical calculations. This point has relevance in the discussion of the NIS 1 calibration and the discussion on the identification of the 335.339 Å line given in Chapter 3.

In conclusion, the Fe XII 338.278 Å line *can* be used for density diagnostics in conjunction with any other Fe XII line seen in the same detector, *but* bearing in mind that it is giving overestimated densities.

Fe XIII

The Fe XIII 359.7 Å(359.642 + 359.842 Å) line is close to the Ne V 359.382 Å line, and therefore can be reliably used only in off-limb or active region observations. The same applies to Fe XIII 320.809, which is blended with O III 320.976 Å and Mg IV 320.994 Å.

Fe XIV

Fe XIV has always been a problem in EUV spectroscopy. Although tens of bright Fe XIV lines are present in EUV spectra, especially in active regions, disagreement between observations and theory has been reported by numerous authors. Only very recently, new calculations (*Storey et al.*, 1999) have shed some light on the Fe XIV problem.

One density diagnostic ratio is reported, but should be used with caution, since the Fe XIV 353.83 Å becomes blended with an Ar XVI 353.920 Å line in active region spectra.

Some other density-sensitive ratios with problems

Now, follow some comments on a few of the many density-sensitive lines that are visible in the CDS wavelength range but which present a series of problems.

Ne V 416.194 / 481.3 (or Ne V 416.843 / 481.3) is not easily usable, because the 481.3 Å line is difficult to fit, being almost at the edge of GIS 3, and because it is a blend with a second order Fe XIII line.

CDS observes various O V 2s 2p ^{3}P – 2p^2 ^{3}P transitions around 760 Å (760.444, 758.675, 762.002, 759.439, 760.225, 761.126 Å from the brightest to the weakest) seen in GIS 4, and the strong 629.73 Å line in NIS 2. The ratio of any of the lines seen in GIS 4 with the 629.73 Å line is a good density diagnostic in the range $N_e = 10^{10} - 10^{12}$, but unfortunately the fact that these lines are observed by the two different spectrometers prevents their use. In fact, the O V lines exhibit repeated brightenings, so these lines can be used for diagnostics only if observed simultaneously, which is not possible with CDS. The 761.126 Å line is also a good density-diagnostic in conjunction with any of the other lines of the multiplet, but is very weak and, with the GIS resolution, in the wing of the bright 760.444 Å line. Only SUMER is able to clearly separate these lines, allowing this ratio to be used to derive densities (*Doschek et al.*, 1998a).

The Mg IX 443.973, 448.293, 439.176, 441.199, 443.403 Å lines (ordered from the brightest to the weakest) are density-sensitive at densities lower than 10^9 and their ratio with any of the lines (368.070, 706.060, and 749.551 Å) could be used as a diagnostic. Unfortunately, aside from calibration problems, these lines are weak and partly blended with first and second order lines, which limits their use.

The Fe XI 308.548 Å line is density-sensitive and could be used in conjunction with e.g. the 369.153 Å line, but it is a weak line, at the edge of NIS 1, probably blended, and in the case of GIS 2, probably affected by *ghosting* problems (see Chapter 3).

Concluding comments

Although the CDS instrument potentially has many density-diagnostic capabilities, unfortunately for various reasons only some of these can be reliably used. Most of them are observed in the NIS 1 channel, which has a low sensitivity and suffers from scattered light (see Chapter 3 for details). The lines observed by the GIS have large uncertainties because of various anomalies and detector effects (see Chapter 3 for details).

Many of the usable density-sensitive lines are emitted at high temperatures, and are hardly visible in coronal holes. Here, sufficient signal-to-noise can only be achieved at the expense of spatial and/or temporal resolution. The Si IX [349.9 Å/ 341.9 Å] ratio is the best density diagnostic for typical coronal hole densities. This ratio varies by a factor of 2 over a variation in density of a factor of 6, (at $N_e \simeq 2 \cdot 10^8$ cm^{-3}). These lines have the added advantage that they are close in wavelength and any error due to the instrumental calibration is minimized. Other line ratios mostly used in this thesis for coronal densities are Si IX [349.9 Å/ 345.1 Å] and Si X [356. Å/ 347.4 Å] . Transition region densities have been estimated principally using the Mg VII [319.0 Å/ 367.7 Å] and the O IV [625.9 Å/ 608.4 Å] ratios.

2.2 The *L-function* method of determining electron density

This diagnostic method allows an evaluation of density and of possible errors in the relative intensity calibration of lines seen at different wavelengths at the same time, comparing lines emitted by the same ion. This method is described by *Landi et al.* (1997a). Briefly, a reasonable assumption is that the *contribution function* can be written in the form:

$$G_{ij}(T, N_e) = f_{ij}(T, N_e)g(T) \tag{2.1}$$

where $g(T)$ is the temperature dependence that mainly comes from the ionization equilibrium and for each ion is the same for all the lines. If an effective temperature T_{eff} is defined:

$$LogT_{eff} = \frac{\int g(T)\ DEM(T)\ logT\ dT}{\int g(T)\ DEM(T)\ dT} \tag{2.2}$$

the function $L_{ij}(N_e)$ (hereafter *L-function*) can be defined as the ratio between the observed line intensity $I_{\rm ob}$ and $G_{ij}(T_{eff}, N_e)$, calculated as a function of N$_e$ at the temperature T_{eff}:

$$L_{ij}(N_e) = \frac{I_{\rm ob}}{G_{ij}(T_{eff}, N_e)} \tag{2.3}$$

The diagnostic method relies on the observation that if all the L-functions of the same ion, calculated with the line fluxes derived from a well-calibrated spectrum, are displayed in the same diagram versus the electron density, all the curves should meet in a common point $(N_e^\star, L(N_e^\star))$. Moreover, the L-functions of density-independent lines should be superimposed. An example of this behaviour is shown in Figure 2.3. It is important to note also that unsplit multiplets of the same ion share this common behavior. The first step is to calculate a DEM. The second step is to compute the effective temperature T_{eff}, which depends on the DEM distribution, for each line of each of the ions. The third step is to display the L-functions at that effective temperature versus electron density in order to verify line overlapping (for density independent lines) or proper crossing (for density dependent ones).

When this procedure is applied to a set of density-sensitive observed lines, the electron density of the emitting plasma may be found. It is possible that some L-functions do not cross the meeting point. In this case, one possible cause is an intensity calibration problem. Thus, it is possible to define an intensity correction factor for all the lines whose L-functions do not intersect at the common crossing point. Lines of the same ion which are observed in more than one spectral window can therefore be used for inter-calibration purposes. This method is particularly useful because it is not strongly dependent on the DEM distribution, and at the same time allows an evaluation of the electron density and the relative calibration to be made, using any number of lines, thereby reducing possible errors compared with using only line ratios.

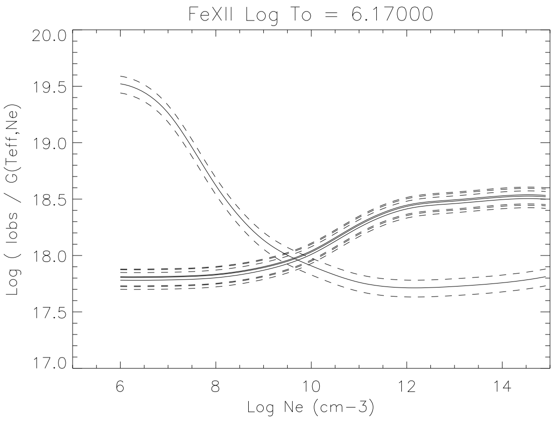

Figure 2.3: *Fe XII lines observed in CDS NIS 1 spectral range. The nearly coincident curves are from lines observed at 346.8 Å, 352.1 Å and 364.4 Å while the crossing transition is observed at 338.2 Å. In each case the dashed lines correspond to the error bars. Courtesy of E. Landi.*

2.3 The electron temperature evaluation. The isothermal case

Estimates of coronal temperatures (averages over the line of sight) can be obtained from ratios of lines emitted by ions of the same element and close ionization stage, assuming that the plasma is isothermal. As already mentioned in Chapter 1, many works have used lines emitted by *different elements*, because of the paucity of the observed spectral lines, introducing extra uncertainties due to abundance estimation. As for the density case, many works have been published on the subject of electron temperature evaluation. A review of some methods is given in *Mason and Monsignori Fossi* (1994), while the above cited work of *Keenan* (1996) gives a useful bibliographical list.

Once the isothermal assumption is made, it is straightforward to deduce from a line ratio a temperature T_*, since the intensity ratio I_1/I_2 is directly equal to the ratio of the contribution functions:

$$\frac{I_1}{I_2} = \frac{C_1(T_*, N_e)}{C_2(T_*, N_e)} \tag{2.4}$$

Any ratios of lines of ions of close ionization stage can be used for this purpose, as long as the lines are not density-sensitive, otherwise the derived temperature T_* becomes density-dependent. A set of IDL routines has been written by the author to calculate the contribution functions, take into account possible blends, and calculate the ratio of $C(T)$s and the temperature from input intensities. Figure 2.4 shows as an example the contribution functions of a Mg VII and a Mg IX line, and how their ratio varies with temperature.

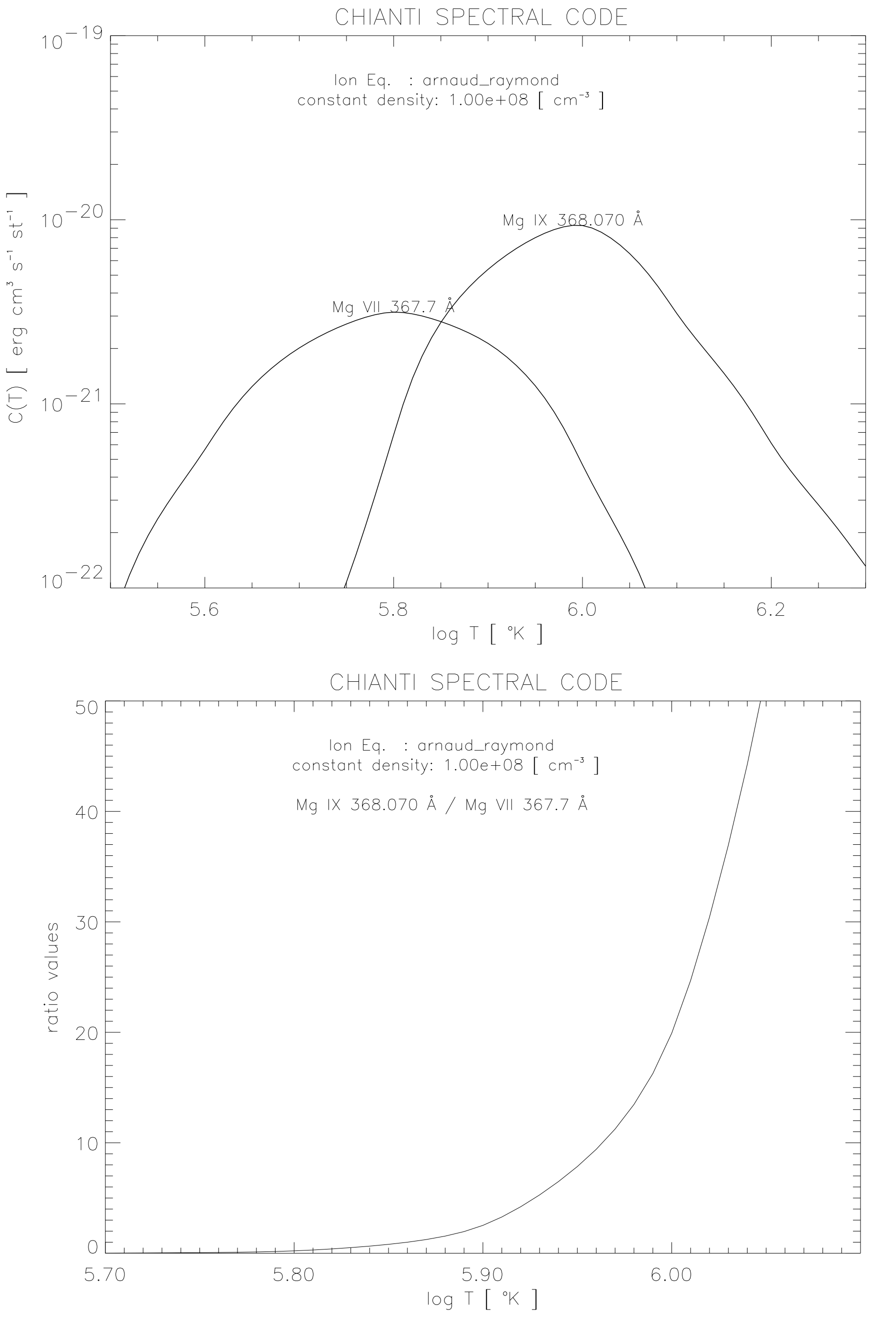

Figure 2.4: *Contribution functions of two Mg VII (a self-blend of two transitions) and Mg IX lines with their ratio, calculated with* Arnaud and Raymond *(1992).*

Different line ratios are expected to give different temperatures, if the plasma distribution is not isothermal. If the plasma distribution along the line of sight is multithermal, as can be expected especially in the case of on-disc observations, isothermal temperatures are only a crude approximation and a more complete description of the distribution of plasma at different temperatures can only be given by the DEM distribution.

Given the fact that CDS observes many emission lines of the same element for different ionization stages, it is possible to choose many useful ratios as temperature diagnostics, using bright lines that are not (or only slightly) density-sensitive. Examples will be given throughout this thesis. Since the emission in high-temperature lines inside coronal holes is very low, the best lines to use are those that are formed at temperatures around a million degrees or lower, for example, [Mg X 624.9 Å/ Mg IX 368.0 Å] and [Mg IX 368.0 Å/ Mg VII 367.7 Å] .

Aside from the cited possible errors due to density and element abundance uncertainties, which can easily be avoided by careful choice of lines, there is one substantial source of error that surprisingly has always been neglected in the EUV literature, except in a few cases. This is the validity of the adopted ionization equilibrium. In fact, the use of different ionization equilibrium calculations produces significantly different results. An example is shown in Figure 2.5.

A more direct way to deduce electron temperatures is to use the ratio of two lines of the same ion. There are only very few cases in which there is a temperature dependence between two lines emitted in the same EUV spectral region. In fact, usually the lines fall at very different wavelengths, as explained in Chapter 1, and are observed by different instruments, increasing the uncertainty in the derived values. An investigation of the lines observed by CDS has shown that Mg IX and Si XI are probably the only ions suitable for this purpose. Some useful Mg IX and Si XI ratios are shown in Figure 2.6.

The ratio of the Si XI 580.9 Å to either the Si XI 303.3 Å (seen in second order in NIS 2) or the Si XI 604.15 Å is temperature-sensitive. The difficulties in using these lines are the following: the 580.9 Å line is partly blended in on-disc observations with O II; the 303.3 Å line on-disc is in the wings of the strong He II 303.8 Å line seen in second order; the use of the 303.3 Å line requires an accurate second order calibration; the 604.15 Å line is weak. Furthermore, the Si XI emission is in practice absent in coronal holes, and very weak in quiet sun conditions.

The Mg IX 368.070, 706.060, and 749.551 Å lines are basically density-insensitive but have a different temperature dependence. Therefore, any combination of any two of these three lines is a good temperature diagnostic. The 706.060, and 749.551 Å lines are seen in GIS 4,

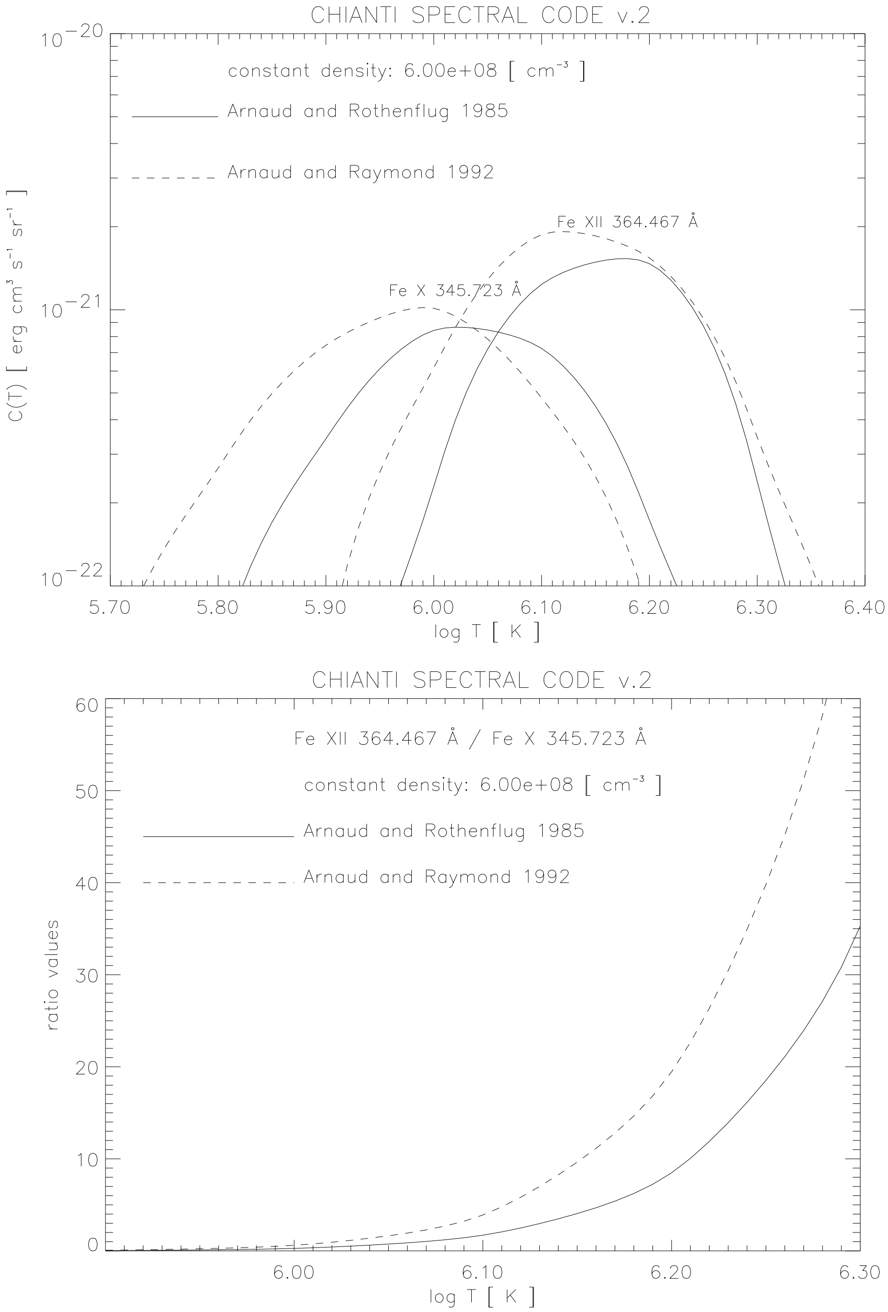

Figure 2.5: *Contribution functions of two iron lines and their ratio, for different ionization equilibria. Note how the ratio is different.*

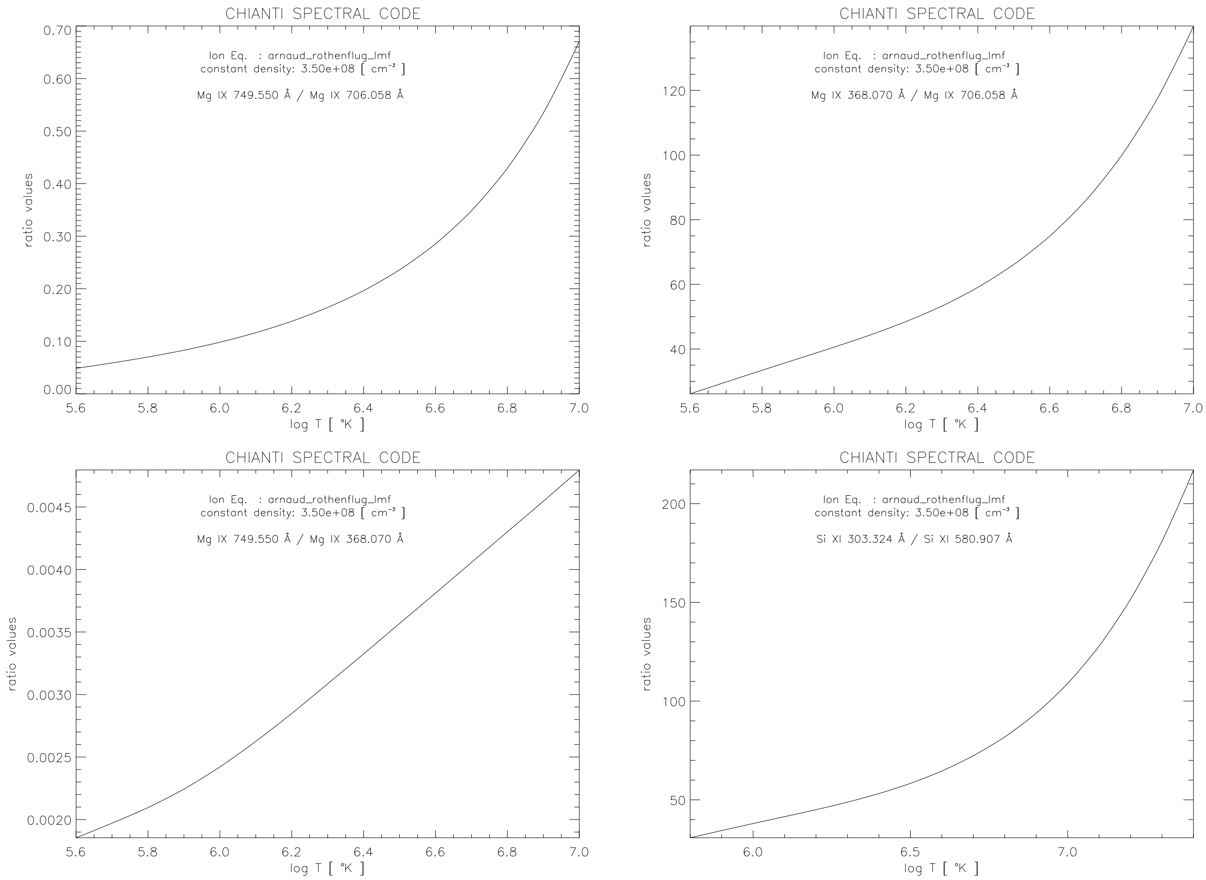

Figure 2.6: *Some useful Mg IX and Si XI temperature ratios, calculated with* Arnaud and Rothenflug *(1985).*

and have been already used as a temperature diagnostic in coronal holes (*Wilhelm et al.*, 1998). GIS 4 also observes a weak line at 694.005 Å that is strongly density-dependent above 10^8 cm^{-3} and also temperature-dependent, but is blended with the much stronger Si IX 345.1 Å seen in second order. Unfortunately, the 749.551 Å line is very weak, and the 706.06 Å line is very close to other lines, making the intensity of the line difficult to measure. The 368.07 Å line is seen in NIS 1 in first order and in GIS 4 in second order, and has the best counting statistics of the three Mg IX lines. The use of the 368.07 Å line is therefore strongly dependent on the inter-calibration between NIS 1 and GIS 4, and the second order calibration of GIS 4.

Details on the calibration and the possible use of the Si XI and Mg IX lines will be given in Chapter 3.

2.4 The electron temperature evaluation. The DEM method

The CDS instrument for the first time offers the opportunity of observing a large number of emission lines emitted over a large temperature range, thus enabling a more complete DEM analysis to be performed than ever before. An example of the span of temperatures covered simultaneously by a wide range of ions observed by CDS is shown in Figure 2.7. Skylab's S082A instrument was capable of observing a large range of ions but was limited by the overlapping in wavelength, while other instruments like the SERTS rockets had limited spatial information (typically only one slit position). This is why a large effort was put into developing methods of DEM analysis for this thesis.

The DEM analysis has also been used in this thesis to deduce relative element abundances. For each element, it is possible to deduce a DEM in the temperature interval for which there are observed emission lines, assuming that the element abundance does not vary along the line of sight. Since the lines observed by CDS are produced by a large number of ions (see e.g. Table 4.2) that cover a large temperature range, it is possible to deduce a DEM curve for each element, and to determine element relative abundances, aligning the DEM curves of the different elements. More details on how the DEM method can be applied will be given in Section 2.5.3 with a practical example, in Section 2.6, and in the following Chapters.

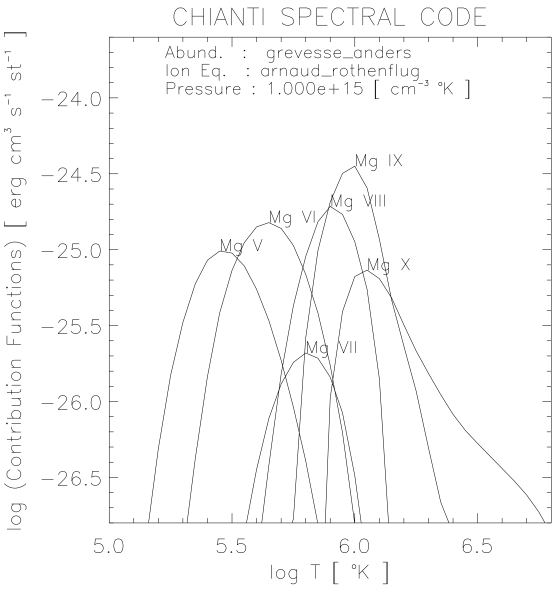

Figure 2.7: *The contribution functions for various ionization stages of Mg: Mg V (353.09 Å), Mg VI (349.1 Å- multiplet), Mg VII (363.77 Å), Mg VIII (315.04 Å), Mg IX (368.07 Å), Mg X (624.94 Å) calculated at constant pressure and with the* Arnaud and Rothenflug *(1985) ionization equilibrium.*

There are various methods of obtaining the differential emission measure. The inversion problem itself is not simple and requires some assumptions about the nature of the solution. A series of workshops was sponsored in 1990/91 to study differential emission measure techniques (*Harrison and Thompson*, 1992). It was found that most codes eventually gave consistent results, but that the DEM derived depends rather critically on the methods used to constrain the solution and the errors in the observed intensities and atomic data.

It is advisable to select a number of well resolved, unblended lines which are not density sensitive, emitted by various elements over a wide temperature interval. Appropriate values of the pressure (or density) and the elemental abundances must be chosen according to the region of the Sun being observed. The pressure value can be obtained once the values of the temperature and the density are estimated.

The inversion technique developed to calculate the DEM

The moderate CDS spectral resolution does not allow all the lines to be resolved. Therefore, a method to take into account all the theoretical lines that might contribute to each observed line had to be developed. If the elemental abundances are assumed constant over the emission volume, for every observed line in a wavelength bin $\Delta\lambda$, the flux observed can be written :

$$I^{ob}_{\Delta\lambda} = \int G_{\Delta\lambda}(T)\ DEM(T)\ dT \tag{2.5}$$

Where $G_{\Delta\lambda}(T)$ is the sum of the contribution functions of all the theoretical lines $G_{\Delta\lambda}(T) = \sum_{\lambda_{ij}} G(T, \lambda_{ij}, N_e)$ within $\Delta\lambda$.

Once the line fluxes $I^{ob}_{\Delta\lambda}$ are measured and the contribution functions $G_{\Delta\lambda}(T)$ are calculated, there are various methods to deduce the differential emission measure.

A set of IDL routines was written in order to evaluate the DEM distributions, using the CHIANTI database. Because of the large number of emission lines observed by the spectroscopic instruments on board SOHO, in particular CDS, there was a need for a semi-automatic set of programs that could allow a quick analysis of the data. A complete set of routines was written, documented and then released for public use into the CDS software. The main routine is called CHIANTI_DEM (see the CDS software note No. 50, *Del Zanna et al.*, 1997 for a description).

A far more complex set of IDL routines was also written for use in this thesis, and is briefly outlined below. The main differences between this and the routines released for public use are more flexibility and interactive control over the various parameters of the fit, and also in the way the fitting is performed. These IDL routines were also used for the intensity calibration work described in Chapter 3, and accepted as input line intensities in *photon-events*, rather than physical units ($ergs\ cm^{-2}s^{-1}sr^{-1}$). The main input to these routines is a file that lists, for each observed line:

- the observed wavelength $\lambda_{\rm ob}$ [Å].
- The observed flux I_{ob} and the corresponding error σ_{ob}.
- The value of $\Delta\lambda$ [Å], corresponding to the spectral resolution of the instrument at that wavelength.
- The identification of the line.
- A flag to indicate if the line is to be used in the fit or not and another one to indicate if the line is a first order line (free from second order contributions) or a second order line (free from first order contributions).

Having read the observed intensities, the routines proceed as follows. First, in the case of GIS lines, a reconstruction of the lines that were *ghosting* is performed (see Chapter 3). Then, the appropriate intensity calibration is applied, converting the intensities to $ergs\ cm^{-2}s^{-1}st^{-1}$, for the first order lines and the second order ones, separately. After this, the CHIANTI database is searched for all the theoretical lines that may have contributed to the observed lines, i.e. that have a theoretical wavelength $\lambda_{\rm th}$ in a $\lambda_{\rm ob} \pm \delta\lambda$ interval. For each line the contribution function $C(T, \lambda_{ij}, N_e)$ is calculated using one ionization equilibrium calculation, either at constant pressure or at constant electron density. This is done in various ways, either directly reading the database or reading files of $C(T, \lambda_{ij}, N_e)$ already prepared, in order to save computing time. The $C(T, \lambda_{ij}, N_e)$ values are calculated for the temperature interval log(T)= 4.0 - 8.0 in steps of log(T) = 0.1. If a constant pressure is selected, $C = C(T, \lambda_{ij}, P/T)$, i.e. for each line the contribution function at the temperature T_i is calculated at an electron density N_e equal to the ratio of the pressure and the temperature T_i. The $C(T, \lambda_{ij}, N_e)$ values corresponding to the observed lines are then stored in an output file, that is used for subsequent DEM evaluations. This method was chosen, because it allowed a fast re-calculation of the DEM changing various parameters (e.g. the element abundances or the lines used in the fit) without having to start again and read the CHIANTI database, which can take a long time (of the order of 20 minutes for a typical set of observations). Also, in some cases some transitions can be missed by this automatic procedure, for example if the wavelength calibration was not very accurate, and have to be subsequently added manually. On the other hand, sometimes some contributions have to be removed.

Once the $C(T, \lambda_{ij}, N_e)$ are calculated, an abundance file is read, containing the values of the elemental abundances, relative to hydrogen. It is possible to change these values. Then the $G(T, \lambda_{ij}, N_e)$) are calculated, multiplying each theoretical line by the abundance factor. It is then possible to check which theoretical lines are contributing to each blend. This is an important step, since in many cases, depending on the density and chemical composition of the plasma along the line of sight , different theoretical lines contribute most to the observed line (see e.g. Figure 2.8 for an example). The same check is performed later during the fit, because in many cases the temperature distribution is the major effect.

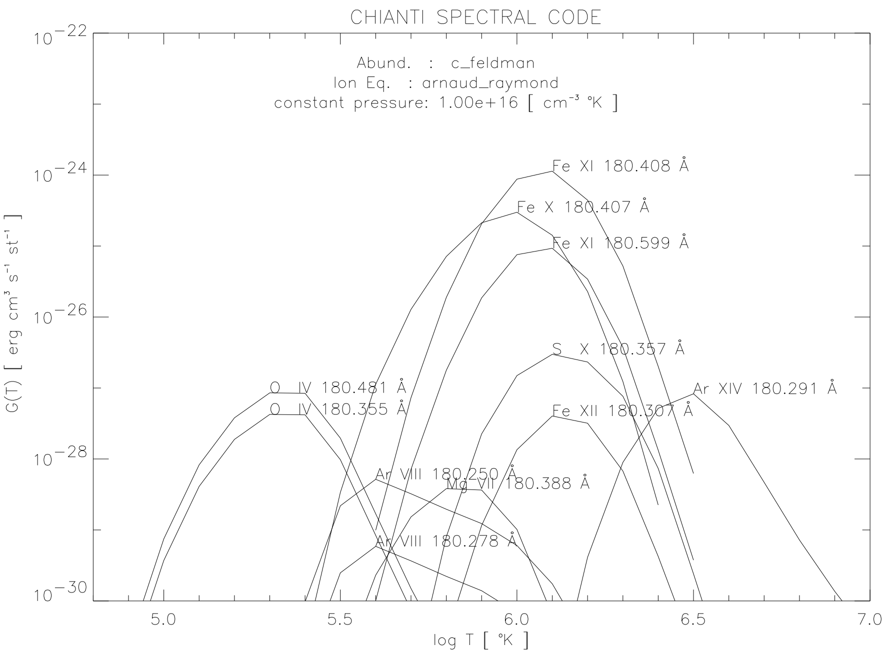

Figure 2.8: *The contribution functions of lines contributing to the observed emission line at 180.4 Å.*

The total contribution function for each observed line is then calculated summing all the theoretical contributions with the abundance factors: $G_{\Delta\lambda}(T) = \sum_{\lambda_{ij}} A_b(X) \cdot C(T, \lambda_{ij}, N_e)$. The inversion of the system of eqns.(2.5) can then start. The numerical inversion procedure used to evaluate the DEM function is an application of the 'maximum entropy method', as described in *Monsignori Fossi and Landini* (1991). The DEM function is assumed to be a cubic spline with a limited number of selected reference ('mesh') points. The smoothness of DEM distribution depends on the number of selected mesh points, which are chosen at those temperatures where there are constraints from observations. This procedure has the advantage to give only positive DEM values and proved to be quickly converging. The fitting program has been modified in order to allow the search for the best solution for each single mesh point, with the possibility of adjusting interactively the number and position of the mesh points. The solution (i.e. the DEM distribution) strongly depends on the correct intensity calibration, the lines used and the adopted element abundances. Since the contribution functions are for each case calculated at the appropriate pressure (or density), also most of the lines that have a slight density-dependence are usually well fitted. Once an appropriate DEM is found, it is then possible to calculate the CDS synthetic spectra, including all the second order contributions, in order to check if, overall, the spectra are well represented or not. This process is usually repeated a few times, adjusting the mesh points and the element abundances to produce the best agreement between observed and calculated intensities.

Regarding possible errors in the estimation of the DEM values, it has been shown by *Dere* (1978b) that if the DEM is approximated with a non-negative smooth function, then the solutions have errors that are not significantly greater than the errors in the spectral data, in the temperature ranges where there are observational constraints. In the regions with limited observational constraints, the DEM values can have large errors, as shown by *Jakimiec et al.* (1984).

2.5 A comparison of various emission measure methods, using Skylab coronal hole data

There are many emission measure methods and definitions to be found in the literature, which can create confusion. For example, in some cases, column emission measures instead of volume emission measures are used. In this Section, the main methods that can be found in the literature are explained, bearing in mind that in each paper the practical definitions are usually different. This is accomplished by applying the DEM analysis described above to a set of data and making a comparison with other methods, to clarify the differences, which in some cases are subtle. At the same time the practical description of how the DEM is applied and of how the results are presented will be given, with various definitions that then will be used in the remainder of this thesis. This is particularly important, since the DEM inversion method will be applied to the CDS data both for calibration and for plasma diagnostic purposes in the following chapters.

In order to present a comparison that is independent of atomic data and instrument calibration, the method is applied to the published Skylab data of *Vernazza and Reeves* (1978), using the same atomic data (CHIANTI v.2) that are used in the analysis of CDS data. As already mentioned, the *Vernazza and Reeves* (1978) data were among the best sources of EUV spectra before SOHO, and have been accurately calibrated in intensity and used by a large number of authors. Only rocket flights such as SERTS have similar accuracy in calibration with a much better resolution, compared to that ($\simeq 1.6$ Å) of the

HCO instrument on-board Skylab. The SERTS data are not used here for the comparison because of the more restricted temperature coverage of the observed lines.

Vernazza and Reeves (1978) produced line intensities for different solar regions. The averaged values for the coronal hole cell centres have been selected for the comparison, so the results can also be useful for various reasons. First, it is interesting to compare the coronal hole DEM derived using the latest atomic data, with previous results. Then, it will be possible to compare this result with that derived from SOHO/CDS data, using the same atomic data, and to point out similarities and differences in where the model fails to reproduce the observations.

The averaged intensities of most of the published lines have been used, in some cases correcting the observed wavelength in order for the automatic routine to find the correct theoretical lines. This has been necessary since the HCO wavelength calibration was poor ($\simeq$ 1-2 Å), of the order of the resolution. A $\Delta\lambda = 1.1 \simeq 0.7 \times FWHM(\text{Å})$, was chosen to ensure that all the significant theoretical contributions would be included. A 10% error on all the observed intensities has been adopted. While this error is reasonable for most of the bright lines, it might be low for the other ones, in particular for those at the shorter wavelengths, where the intensity calibration becomes more uncertain. The contribution functions have been calculated at constant pressure $P = 2 \times 10^{14}\text{cm}^{-3}$ K with the ionization equilibrium calculations of *Arnaud and Rothenflug* (1985). The inversion technique described above was applied to these data in order to derive the DEM. As a starting point, photospheric abundances of *Grevesse and Anders* (1991) were used, but some element abundances were then slightly changed, as described below. These abundances are referred to as the *adopted abundances* for this work, and are the photospheric except for Ne, Ca and Na, for which the values were increased from the photospheric ones by 0.2, 0.2, 0.4 (in logarithmic scale), respectively.

Only some *selected* observed lines emitted by different ions are shown here, for clarity, bearing in mind that many other lines (most of which are in agreement with the selected ones) were included. Figure 2.9 shows the composite contribution functions G(T) for these lines (see Table 2.2 for the identifications), showing the large temperature coverage, which is only limited at high temperatures, where no reliable lines were observed. It also shows that some of the G(T) are *not* sharply peaked, because of the ionization equilibrium, as is the case for some ions like Si III and O VI, or because of blending, as in the case of Mg IX. In many cases the G(T) are even double-peaked, with peaks at low and high temperatures as is the case of the Ca X – C III blend observed at 574.2 Å. In such complex cases, which are quite common, it is not easy to find the contribution of each line to the blend, because it strongly depends on the DEM values around the temperature of the maximum of the

C(T) of each contributing line (log T_{max} = 5.8 for Ca X and log T_{max} = 5.0 for C III), and on the relative element abundance, so only a proper *DEM* and abundance analysis can give the correct answer. Figure 2.9 also shows that in some cases, such as the pairs O III, Ne III and O IV, Ne IV the contribution functions have almost the same temperature dependence, and therefore are suitable for element abundance analysis, as described in Section 2.5.3.

Recalling that the theoretical intensity of a line can be written (see Chapter 1), assuming constant abundances along the line of sight as

$$I_{\mathrm{th}} = A_b(Z) \int_h C(T, N_{\mathrm{e}})\ N_e N_H\ dh = A_b(Z) \int_T C(T, N_{\mathrm{e}})\ DEM(T)\ dT \tag{2.6}$$

the solution to the inversion problem is to use the observed intensities I_{ob} and derive at the same time the element abundances $A_b(Z)$ and the differential emission measure DEM.

2.5.1 Some historical approaches. The EM_L, EM_T, DEM_L approximations

In the past, various approaches have been used to obtain estimates of emission measure distribution and element abundances A_b(Z).

The emission measure loci approach

One direct approach is to plot the ratio $I_{\mathrm{ob}}/G(T)$ for each line as a function of temperature and consider the loci of these curves to constrain the shape of the emission measure distribution. In fact, for each line and temperature T_i the value $I_{\mathrm{ob}}/G(T_i)$ represents an upper limit to the value of the *line emission measure* EM_L (Equation 2.8, below) at that temperature, assuming that all the observed emission I_{ob} is produced by plasma at temperature T_i. An example of such an approach applied to solar EUV spectra can be found in *Judge et al.* (1995).

The $I_{\mathrm{ob}}/G(T)$ curves for the selected lines of the coronal hole spectrum are displayed in Figure 2.10. An examination of the Figure shows already the main expected characteristics of an emission measure from on-disc observations, i.e. a minimum at lower transition region temperatures, and a maximum around a million degrees.

Note that with the adopted abundances the O III/Ne III and O IV/Ne IV curves overlap almost exactly, which confirms that the relative adopted O/Ne abundance is correct.

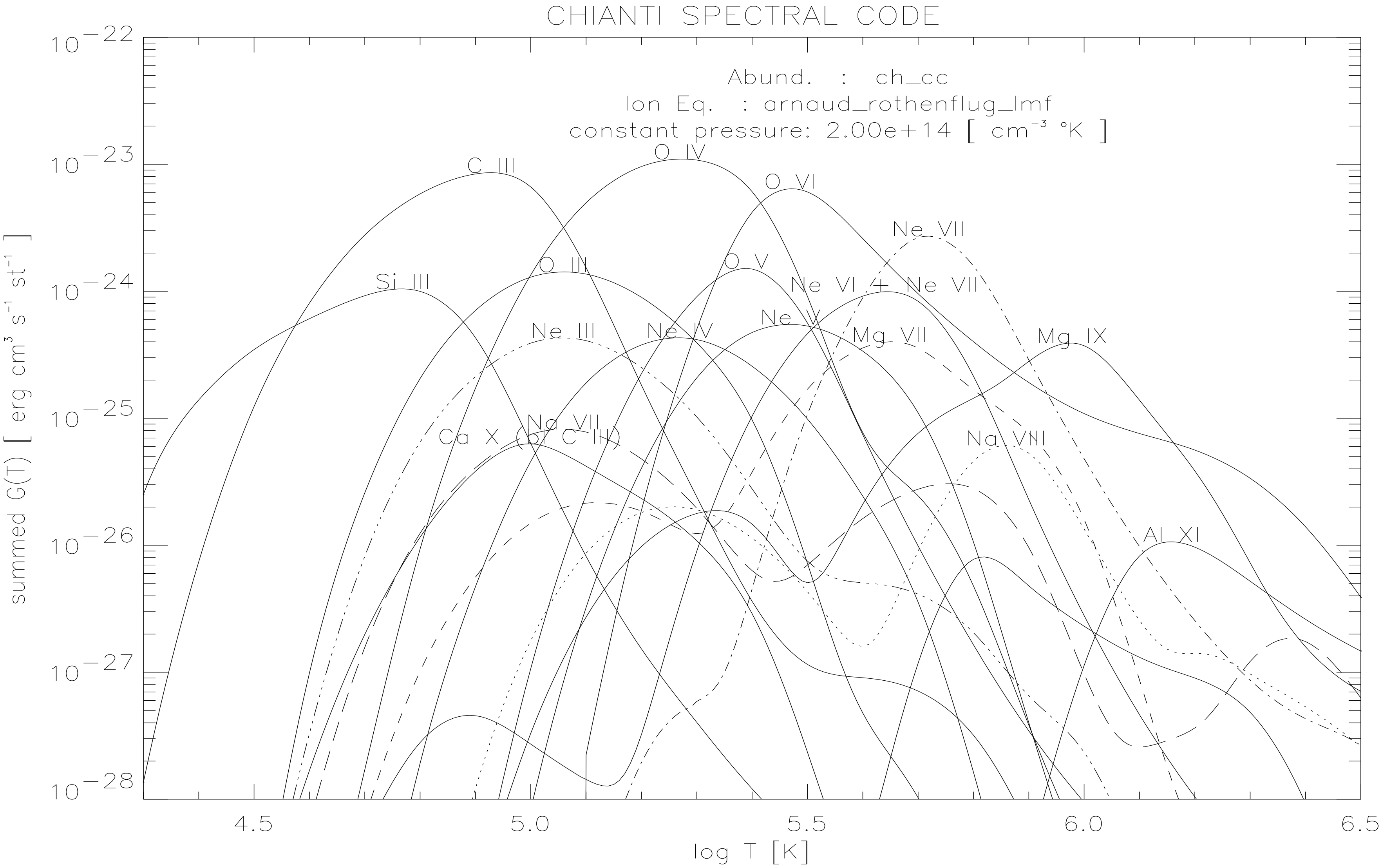

Figure 2.9: *Contribution functions $G(T)$ of the selected observed lines, calculated with the adopted abundances.*

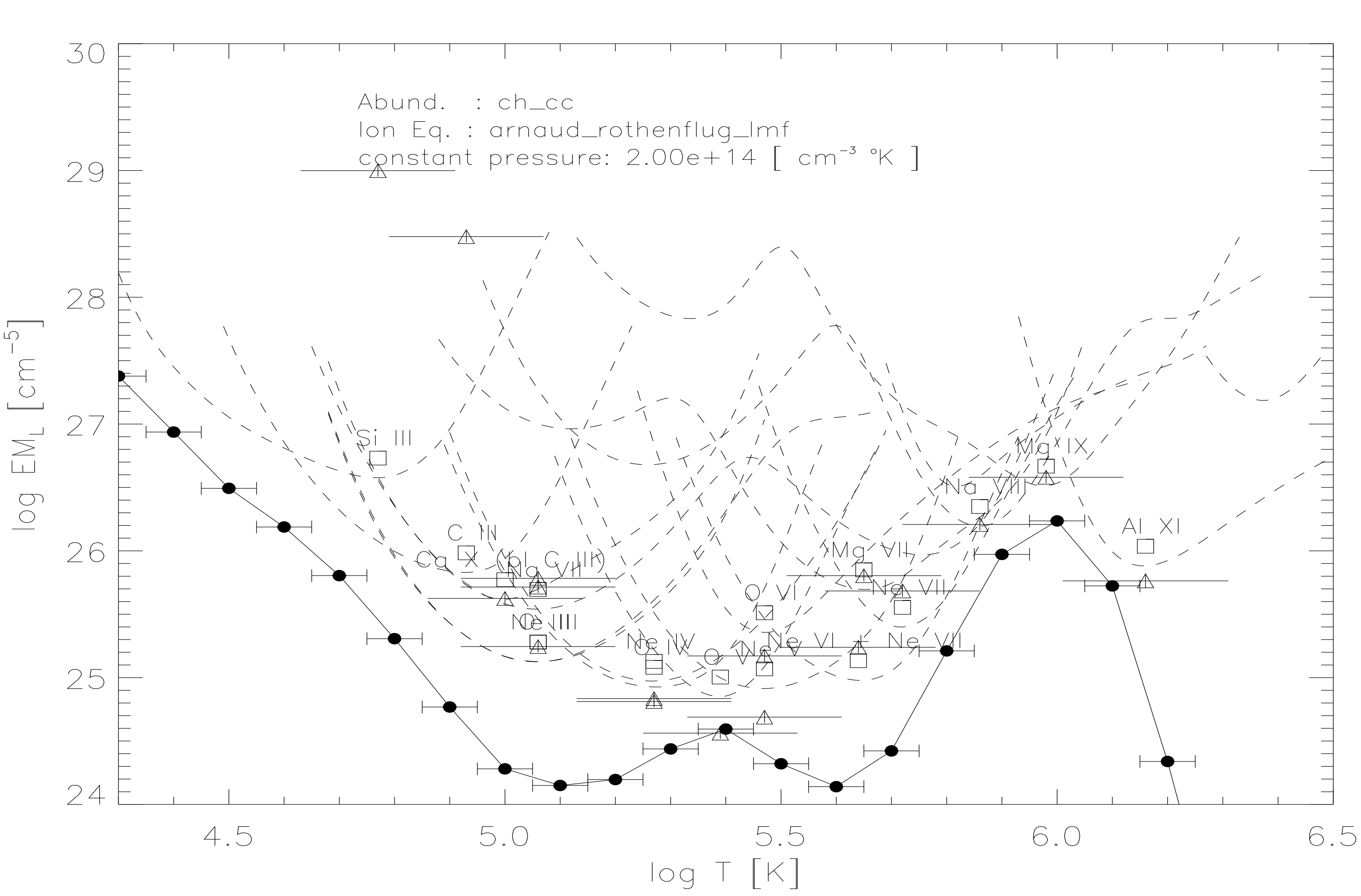

Figure 2.10: *The emission measure values of the selected observed lines, calculated with the adopted abundances. Values of* EM_L Pottasch *(1963) are represented by squares, while the EM(0.3) values (*Jordan and Wilson, *1971) are triangles, both plotted at the temperature* $T_{\max}$. *The horizontal bars of the EM(0.3) values are* $\Delta logT = 0.3$ *K wide. Filled circles represent the* EM_T *values calculated from the DEM. The horizontal bars refer to the adopted* $\Delta logT = 0.1$ *K for the calculation of the* EM_T *values.*

The *Pottasch* approach

Following *Pottasch* (1963), many authors (e.g. *Dupree*, 1972) have approximated the above expression (Equation 2.6) by removing an averaged value of C(T) from the integral:

$$I_{\rm th} = A_b(Z) \ < C(T) > \int_h N_e N_H dh \tag{2.7}$$

A suitably defined volume *line emission measure* EM_L can therefore be defined, for each observed line of intensity $I_{\rm ob}$:

$$EM_L \equiv \frac{I_{\rm ob}}{A_b(Z) \ < C(T) >} \quad [{\rm cm}^{-5}] \tag{2.8}$$

Now, the crude approximation applied by *Pottasch* (1963) was to take $C(T) = 0$ when $C(T)$ is less than one-third of its maximum value, and equal to a constant value otherwise. For T_1, T_2 such that $C(T_1) = C(T_2) = \frac{1}{3}C(T_{\rm max})$, define:

$$C_P(T) = \begin{cases} C_0 & T_1 \leq T \leq T_2 \\ 0 & T < T_1, \quad T > T_2 \end{cases} \tag{2.9}$$

and requiring that

$$< C(T) >= \frac{\int C(T) dT}{|T_2 - T_1|} \tag{2.10}$$

gives $< C(T) >= 0.7\ C(T_{\rm max})$. Since each spectral line is emitted from a volume V, over a temperature range $T_2 - T_1 = \Delta T$ around the temperature $T_{\rm max}$ corresponding to the peak value of its contribution function, $C(T_{\rm max})$, *Pottasch* (1963) and following authors have produced figures of the *line emission measures*, multiplied by the corresponding abundance value:

$$A_b(Z)\ EM_L = \frac{I_{\rm ob}}{0.7\ C(T_{\rm max})} \tag{2.11}$$

plotted at the temperature $T_{\rm max}$. The relative abundances of the elements are derived in order to have all the *line emission measures* of the various ions lie along a common smooth curve. This is of course possible only for the observed elements and once one element abundance is fixed.

The *line emission measures* EM_L calculated with this approximation, using the adopted abundances for the selected lines of the coronal hole spectrum are displayed as squares in Figure 2.10.

The *Jordan and Wilson* approximation

Jordan and Wilson (1971) adopted the *Pottasch* (1963) approach but proposed a different approximation, assuming that $C(T)$ has a constant value over a narrow temperature interval $\Delta logT = 0.3$ around $C(T_{\max})$:

$$C_J(T) = \begin{cases} C_0 & |\log T - \log T_{\max}| < 0.15 \\ 0 & |\log T - \log T_{\max}| > 0.15 \end{cases} \tag{2.12}$$

and requiring that

$$\int C(T)dT = \int C_J(T)dT \tag{2.13}$$

so that

$$C_0 = \frac{\int C(T)\ dT}{T_{\max}(10^{+0.15} - 10^{-0.15})} = \frac{\int C(T)\ dT}{0.705\ T_{\max}} \tag{2.14}$$

and thus deducing the relative *line emission measure* EM_L, sometimes indicated by EM(0.3), to make clear that the contributions are calculated over a temperature interval $\Delta logT = 0.3$. This approximation has been used by various authors (for example by *Widing et al.*, 1986, to derive the element abundances of an erupting prominence observed by Skylab).

Values of EM(0.3)for the coronal hole spectrum are displayed in Figure 2.10 as triangles, together with their $\Delta logT = 0.3$ intervals. The agreement with the values deduced from the *Pottasch* (1963) approximation is reasonable for the few lines that are sharply peaked, but is poor for the other ones. It is also evident that, for most of the lines, the emissivities outside the $\Delta logT = 0.3$ interval are *not* negligible.

A way to compare the emission measures derived from these two most commonly used approximations is to calculate some emission measure values as a function of temperature directly from the differential emission measure values, after the DEM has been calculated. As usual, an emission measure has to be defined over some temperature interval ΔT. For each temperature T_i it is therefore possible to define an emission measure value EM_T:

$$EM_T(T_i) \equiv \int_{T_i - \frac{\Delta T}{2}}^{T_i + \frac{\Delta T}{2}} DEM(T)dT \tag{2.15}$$

These EM_T points have been calculated from the DEM distribution (Figure 2.12) with a $\Delta logT = 0.1$, and are displayed in Figure 2.10 with filled circles. It is quite obvious that neither of the two approximations above is a good representation of the emission measure derived from the DEM.

A different approach. The DEM_L method

A different approach was proposed by *Widing and Feldman* (1989). The idea is to rewrite Equation 2.6 in terms of differential emission measure :

$$I_{\rm th} = A_b(Z) \int\limits_T C(T, N_{\rm e})\; N_e N_H \frac{dh}{dT} dT \tag{2.16}$$

and to extract from the integral an averaged value of the DEM of the line, that in this thesis is termed the *line differential emission measure* DEM_L:

$$DEM_L \equiv \left\langle N_e N_H \frac{dh}{dT} \right\rangle \quad [cm^{-5} K^{-1}] \tag{2.17}$$

such that for each line of observed intensity $\mathrm{I_{ob}}$:

$$DEM_L \equiv \frac{I_{\rm ob}}{A_b(Z) \int\limits_T C(T) dT} \tag{2.18}$$

A plot of the $A_b(Z)\; DEM_L = I_{\rm ob} / \int\limits_T C(T) dT$ values displayed at the temperatures $\mathrm{T_{max}}$ gives the differential emission measures of the observed lines, and at the same time can be used (*Widing and Feldman*, 1989) to deduce relative element abundances, adjusting them in order to have a continuous sequence of the $A_b(Z)\; DEM_L$ values.

The DEM_L values for the coronal hole spectrum, calculated with the adopted abundances, are shown in Figure 2.11 at the temperatures $\mathrm{T_{max}}$. This figure shows a minimum of the DEM_L values around log T=5.4, a maximum at a million degrees, and an exact overlap of the Ne III, O III and Ne IV, O IV points, confirming the validity (by using this method) of the adopted relative Ne/O abundance.

This DEM_L approach has been used and reported in almost all the works on element abundance analysis, after *Widing and Feldman* (1989). The method is quick to apply, since it only requires for each line an integration of the contribution function, and apparently gives the correct answer in term of abundance analysis. In reality, it will be shown below that **this method should not be applied to deduce a DEM distribution**, because it is inherently wrong, **nor to deduce elemental abundances**, except in particular cases.

2.5.2 Results of the DEM approach, basic definitions and comparison with the DEM_L method.

The DEM approach assumes that a DEM can be defined, and that it is a smooth function of temperature, which is a basic assumption (well accepted in the literature). The current

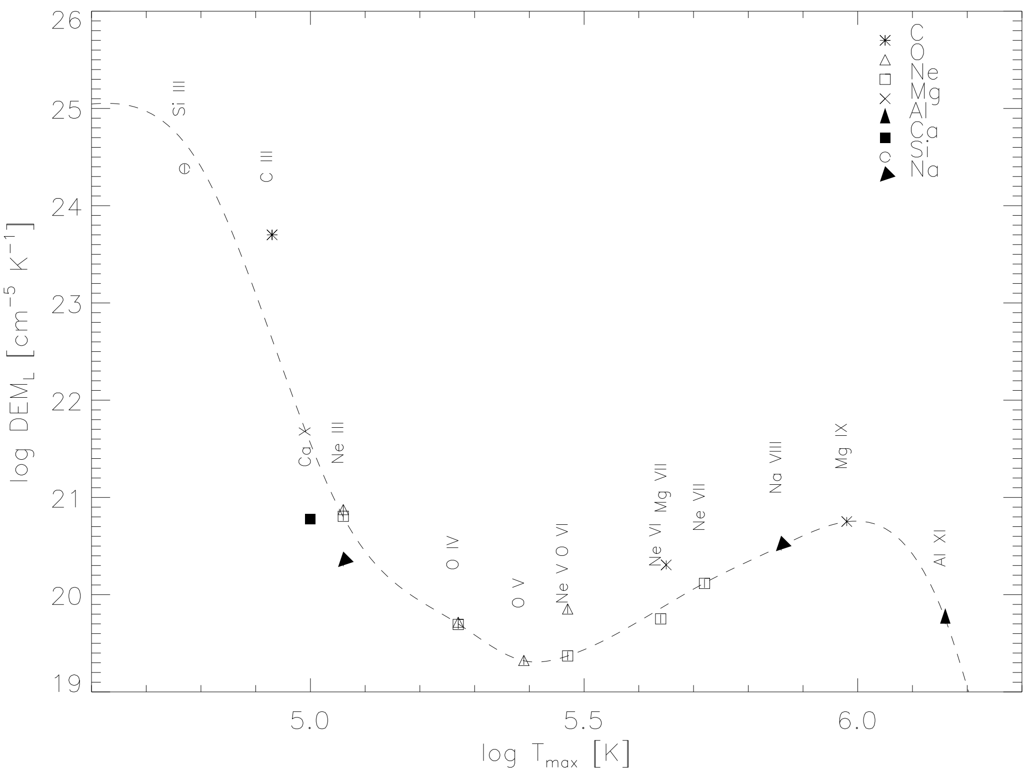

Figure 2.11: *Line differential emission measures DEM_L of selected lines with Skylab data, with the adopted abundances. A 'trial' DEM is plotted as a dashed line. Note that the O III, Ne III and O IV, Ne IV points overlap.*

EUV instruments have such a spatial resolution (of order 2″) that any small-scale features on the Sun have a diffuse aspect. Also, since the emission is optically thin, the sum of all the contributions along the line of sight blurs any contribution from possible filamentary structures.

Figure 2.12 shows the DEM distribution of the Skylab coronal hole cell-centre data, found with the inversion technique. The mesh points, indicated with triangles, are positioned at the temperatures where there are good constraints, i.e. well-observed lines that are emitted at those temperatures. In this case, the high-temperature tail of the DEM distribution is not directly constrained. On the other hand, the absence of observed high-temperature lines in the spectrum is itself an excellent constraint on the upper limits of the DEM distribution at high-temperatures. Any higher values of the DEM at temperatures above 10^6 K would make high-temperature lines observable above the noise. The low-temperature tail of the DEM distribution is directly constrained by low-temperature lines but should be treated with caution, since some opacity effects may come into play.

Now, some definitions that will be used throughout the rest of this thesis: a theoretical

Table 2.2: *Selected lines of the averaged coronal hole spectrum of* Vernazza and Reeves *(1978), with the adopted abundances.*

Ion	λ_{th} (Å)	λ_{ob} (Å)	Transition	I_{ob}	I_{th}/I_{ob}	+/-	log T_{eff}	log T_{max}	frac
With the adopted abundances									
Si III	1206.499	1206.5	3s2 $^1S_0$ - 3s.3p $^1P_1$	393.6	1.33	0.19	4.53	4.77	
C III	977.017	977.0	2s2 $^1S_0$ - 2s2p $^1P_1$	579.4	0.99	0.14	4.73	4.93	
O III	599.597	599.6	2s22p2 $^1D_2$ - 2s2p3 $^1D_2$	19.0	1.02	0.14	4.99	5.06	
Ne III	489.495	489.3	2s2 2p4 $^3P_2$ - 2s 2p5 $^3P_2$	5.7	1.06	0.15	5.06	5.06	0.56
Ne III	488.9		2s2 2p4 $^3P_1$ - 2s 2p5 $^3P_0$					5.06	0.15
Ne III	490.3		2s2 2p4 $^3P_0$ - 2s 2p5 $^3P_1$					5.06	0.15
Ne III	489.6		2s2 2p4 $^3P_1$ - 2s 2p5 $^3P_1$					5.06	0.11
O IV	554.513	554.5	2s2 2p $^2P_{3/2}$ - 2s 2p2 $^2P_{3/2}$	92.7	0.98	0.14	5.30	5.27	0.55
O IV	554.1		2s2 2p $^2P_{1/2}$ - 2s 2p2 $^2P_{1/2}$					5.27	0.22
O IV	555.3		2s2 2p $^2P_{3/2}$ - 2s 2p2 $^2P_{1/2}$					5.27	0.11
O IV	553.3		2s2 2p $^2P_{1/2}$ - 2s 2p2 $^2P_{3/2}$					5.27	0.11
Ne IV	543.892	543.8	2s2 2p3 $^4S_{3/2}$ - 2s 2p4 $^4P_{5/2}$	4.0	0.93	0.13	5.32	5.27	
O V	760.444	760.0	2s.2p $^3P_2$ - 2p2 $^3P_2$	10.7	1.07	0.15	5.40	5.39	0.69
O V	759.4		2s.2p $^3P_0$ - 2p2 $^3P_1$					5.39	0.17
O V	760.2		2s.2p $^3P_1$ - 2p2 $^3P_1$					5.39	0.13
Ne V	572.331	572.3	2s22p2 $^3P_2$ - 2s2p3 $^3D_3$	4.5	1.16	0.16	5.49	5.47	0.85
Ne V	572.1		2s22p2 $^3P_2$ - 2s2p3 $^3D_2$					5.47	0.14
Na VII	491.951	491.9	2p $^2P_{3/2}$ - 2s.2p2 $^2D_{5/2}$	2.8	0.97	0.14	5.69	5.78	0.42
Ne III	491.0		2s2 2p4 $^3P_1$ - 2s 2p5 $^3P_2$					5.06	0.41
Ca X	574.010	574.2	3s $^2S_{1/2}$ - 3p $^2P_{1/2}$	2.6	0.82	0.12	5.72	5.82	0.53
C III	574.3		2s2p $^1P_1$ - 2s3d $^1D_2$					4.98	0.35
Ne VI	562.803	562.0	2s2 2p $^2P_{3/2}$ - 2s 2p2 $^2D_{5/2}$	9.4	1.20	0.17	5.76	5.63	0.66
Ne VII	561.7		2s2p $^3P_2$ - 2p2 $^3P_2$					5.72	0.22
O VI	1031.912	1032.0	1s2 2s $^2S_{1/2}$ - 1s2 2p $^2P_{3/2}$	145.9	0.65	0.09	5.81	5.47	
Ne VII	465.220	465.2	2s2 $^1S_0$ - 2s2p $^1P_1$	68.1	1.03	0.15	5.87	5.72	
Mg VII	434.917	434.6	2s22p2 $^3P_2$ - 2s2p3 $^3D_3$	19.9	0.79	0.11	5.88	5.80	0.67
Ne VI	435.6		2s2 2p $^2P_{3/2}$ - 2s 2p2 $^2S_{1/2}$					5.64	0.21
Mg VII	434.7		2s22p2 $^3P_2$ - 2s2p3 $^3D_2$					5.81	0.10
Na VIII	411.166	411.2	2s2 $^1S_0$ - 2s.2p $^1P_1$	9.6	0.93	0.13	5.93	5.86	
Mg IX	368.070	368.2	2s2 $^1S_0$ - 2s.2p $^1P_1$	127.3	0.94	0.13	5.98	5.98	
Al XI	550.031	550.0	1s2.(^{1}S).2s $^2S_{1/2}$ - 1s2.(^{1}S).2p $^2P_{3/2}$	0.8	0.95	0.15	6.07	6.16	
With the photospheric abundances of *Grevesse and Anders* (1991)									
Ne III	489.495	489.3		5.7	0.67	0.09	5.08	5.06	0.56
Ne III	488.9							5.06	0.15
Ne III	490.3							5.06	0.15
Ne III	489.6							5.06	0.11
Ne IV	543.892	543.8		4.0	0.59	0.08	5.32	5.27	
Ne V	572.331	572.3		4.5	0.73	0.10	5.49	5.47	0.85
Ne V	572.1							5.47	0.14
Ne III	491.040	491.9		2.8	0.48	0.07	5.62	5.06	0.52
Na VII	492.0							5.78	0.33
C III	574.279	574.2		2.6	0.66	0.10	5.64	4.98	0.43
Ca X	574.0							5.82	0.42
Ne VI	562.803	562.0		9.4	0.76	0.11	5.76	5.63	0.66
Ne VII	561.7							5.72	0.22
Ne VII	465.220	465.2		68.1	0.65	0.09	5.87	5.72	
Mg VII	434.917	434.6		19.9	0.73	0.10	5.89	5.80	0.73
Ne VI	435.6							5.64	0.14
Mg VII	434.7							5.81	0.11
Na VIII	411.166	411.2		9.6	0.38	0.05	5.93	5.86	

line is considered a **principal** line if it *contributes at least 10% of the total theoretical* I_{th} *intensity*; an observed line is considered a **blend** *if its emission is composed of at least two principal lines*; an observed line is considered a **self-blend** if all the **principal** lines are of the same ion. Note that with these definitions the same observed line can be considered a blend of different lines or not depending on the importance of the contribution from the various lines, which in turn depends on the DEM distribution (i.e. on the type of observed source on the Sun), the element abundance, and on the ionization equilibrium used. Examples of observed lines that become blends of different principal lines under different conditions will be given throughout this thesis. A line will be termed **well-reproduced** if the calculated intensity I_{th} equals the observed intensity I_{ob}, within the errors.

Table 2.2 shows the details of the selected lines with the adopted abundances and, for comparison, some of the results with photospheric abundances which were used as a starting point.

Note that all the Tables presented in this thesis have the following contents and abbreviations:

- the observed wavelength λ_{ob} in column (3).
- The identification (ion and theoretical wavelength λ_{th}) of *only* the lines that were found to contribute to the observed line, in columns (1, 2). Only *principal* lines are shown.
- The configuration and term of the lower and upper level, in column (4).
- The observed flux I_{ob} ($ergs\ cm^{-2}s^{-1}sr^{-1}$) in column (5).
- The ratio between the theoretical I_{th} and the observed flux I_{ob}, with an estimated error, in columns (6,7). The theoretical I_{th} is calculated summing up all the contribution functions from all the lines in the blend, and integrating the product with the DEM distribution (Equation 2.6). The error is the combination of the observed error (see Chapter 3) and an assumed 10% error on the calculated values.
- The *effective temperature* $\mathrm{T_{eff}}$ of the line, as a $\log_{10}$ value, in column (8). The effective temperature $\mathrm{T_{eff}}$ is defined:

  $$T_{\mathrm{eff}} = \frac{\int T\ G(T)\ DEM(T)\ dT}{\int G(T)\ DEM(T)\ dT} \qquad (2.19)$$

  i.e. is an averaged temperature, weighted by the DEM distribution.

- The T_{max} value of the transition as a $\log_{10}$ value, in column (9), calculated as the temperature of the maximum of the contribution function.

- The fraction, *frac*, the calculated intensity of each transition contributed, to the total theoretical I_{th} intensity of the line, in column (10). Only principal lines are shown.

- (*bl*) indicates when a line is a blend.

- A number in parentheses indicates the number of self-blends.

- IIo indicates a line seen in second order.

The lines in Table 2.2 are ordered by the *effective temperature* T_{eff}. Table 2.2 shows that even with the conservative errors adopted, most of the lines are well represented within the errors, with a few exceptions, one of which is the O VI line, for which more comments will be given later. Table 2.2 also shows that most of the selected lines are blends, a feature common to most of the lines, due to the poor spectral resolution of the HCO instrument.

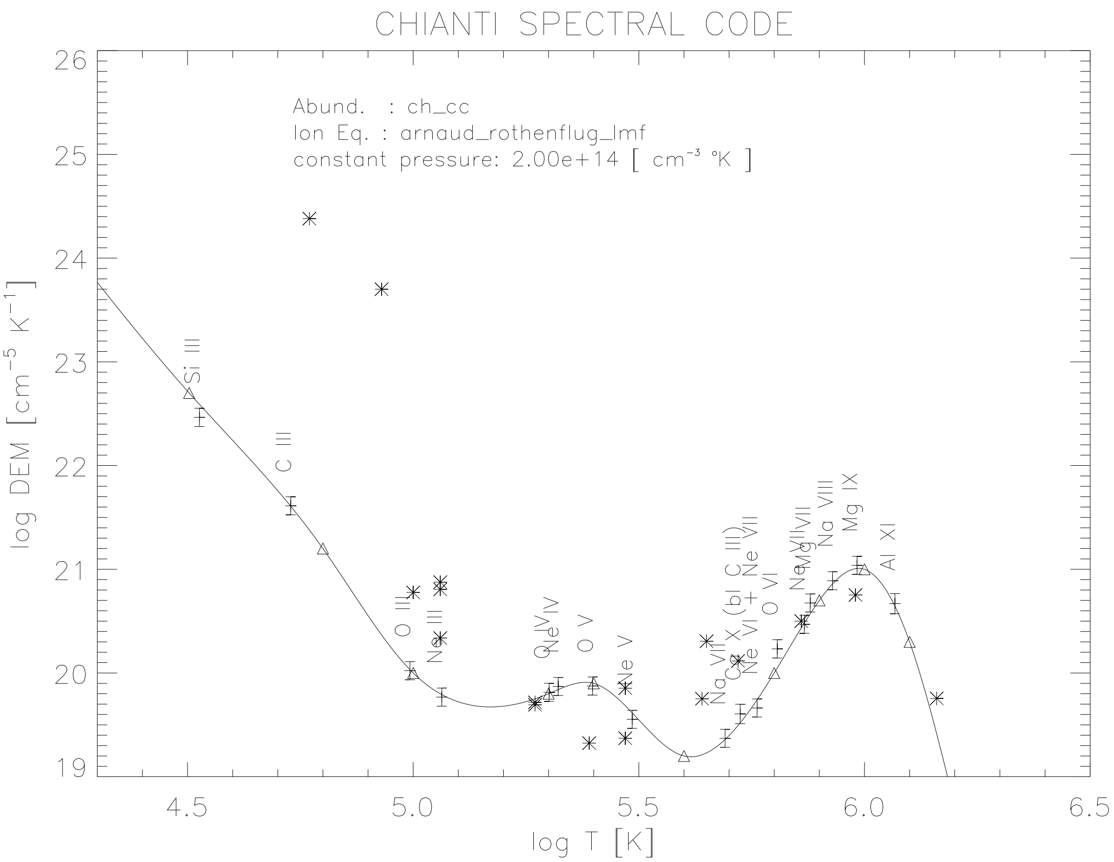

Figure 2.12: *The DEM distribution (continuous line) calculated with the adopted abundances, with the mesh points indicated by triangles. The points with the error bars (labelled with the ion) are plotted at the temperature T_{eff}. Also reproduced with the * symbol are the line differential emission measures DEM_L values of Figure 2.11.*

A comparison of the effective temperature $T_{\rm eff}$ and the maximum temperature $T_{\rm max}$ of the principal lines is instructive. For example, the maximum of the G(T) for the Si III 1206.5 Å line is at log T=4.77 K, but the G(T) of this line is very broad, as shown in Figure 2.9. Since the DEM distribution has a steep increase toward low temperatures, the contribution to the *emissivity* $G(T)$ $DEM(T)$ from temperatures $T < T_{\rm max}$ is very important indeed, and in fact the effective temperature log $T_{\rm eff}$=4.53. A similar case is seen for O VI 1032 Å a line with very broad G(T), but this time the steepening of the DEM distribution is toward higher temperatures, which means that this time most of the observed O VI emissivity comes from plasma at temperatures higher than the maximum of the G(T) (in fact log $T_{\rm eff}$=5.81 while log $T_{\rm max}$=5.47). This also explains why the O VI lines are still visible in off-limb observations, while all the other lines that have peaks of their G(T) around log $T_{\rm max}$=5.5 (as Ne V) are not seen at all. This *shows how graphs that show quantities such as DEM_L as a function of $T_{\rm max}$ can be misleading.* The effective temperature $T_{\rm eff}$ instead gives a much better indication of where the bulk of the emissivity of the lines comes from, at least in some cases.

In order to have a visual representation of the data in Table 2.2, each experimental data point is plotted in Figure 2.12 at the effective temperature $T_{\rm eff}$ and at a value equal to the product $DEM(T_{\rm eff})$×(I_{ob}/I_{th}). *The DEM is therefore not strictly speaking a fit through the points.* The same type of representation is also adopted in the rest of this thesis.

The error bars refer to the combination of observational and theoretical (10%) errors and give an idea of the uncertainties in the derived DEM values. In the same figure 2.12 the EM_L values of Figure 2.11 are also plotted as asterisks, for a direct comparison. This comparison gives a better idea of the large differences in the ordinate values on the one hand, and on the differences between $T_{\rm eff}$ and $T_{\rm max}$ on the other. The worst cases are those of the blends that are composed of principal lines that have peaks in their G(T) at different temperatures, such as the Ca X – C III blend, where the maximum of the total G(T) is at log $T_{\rm max}$=5, i.e. where the C III line has maximum emissivity. In fact, with the adopted abundances, the G(T) of C III is higher than the G(T) of Ca X. But the DEM distribution is such that the emissivity of the Ca X (that peaks at log $T_{\rm max}$=5.8) becomes stronger than that of the C III line, resulting in log $T_{\rm eff}$=5.7. Only a few lines have $T_{\rm max} \simeq T_{\rm eff}$ when $T_{\rm max}$ can be safely used to indicate the region of maximum emission. The reasons for this can be various, but in most cases this happens when: a) such lines have G(T) almost equal (except for a scaling factor); b) *and* most of their G(T) is at temperatures where the DEM distribution is relatively flat, as is the case of the self-blends Ne III, O IV, O V, Ne V. More details of these lines can be found in the following Section.

This explains why the DEM_L method fails when used to estimate the differential emission

Table 2.3: *Some of the selected lines of the averaged coronal hole spectrum of* Vernazza and Reeves *(1978), with the theoretical intensities I_{th} calculated with the adopted abundances and with the trial DEM curve derived from the DEM_L values of Figure 2.11.*

Ion	λ_{th} (Å)	λ_{ob} (Å)	I_{ob}	I_{th}/ I_{ob}	+/-	log T_{eff}	log T_{max}	frac
Si III	1206.499	1206.5	393.6	604.91	86.25	4.66	4.77	
O III	599.597	599.6	19.0	632.44	89.44	4.80	5.06	
O IV	554.513	554.5	92.7	10.37	1.47	4.93	5.27	0.50
O IV	554.1						5.27	0.20
O IV	555.3						5.27	0.10
O IV	553.3						5.27	0.10
O V	760.444	760.0	10.7	0.57	0.08	5.40	5.39	0.69
O V	759.4						5.39	0.17
O V	760.2						5.39	0.13
Ne VII	465.220	465.2	68.1	1.73	0.25	5.80	5.72	
Mg IX	368.070	368.2	127.3	0.67	0.10	5.98	5.98	0.81

measure and the element abundances. When trying to use it to estimate a DEM, this method is inherently wrong because it first assumes that for each emission line the DEM is a constant in temperature (and therefore can be extracted from the integral, Equation 2.6), and then pieces together these values to reconstruct a smooth curve. This simply does not work, even if emission lines with narrow G(T) are used. This can already be seen by the large differences between the DEM_L and DEM values in Figure 2.12. To give a quantitative idea on the differences, which are striking, a smooth curve joining the DEM_L values has been taken as a trial DEM curve (the dashed line in Figure 2.11) and the G(T) of the observed lines folded with it (Equation 2.6), to calculate the theoretical values. The results are shown in Table 2.3. Lines that are in the region of steep DEM gradient such as the Si III 1206.5 Å line are overestimated by a factor of 600. Even lines that do not have a wide G(T) such as the O IV 554.5 Å line *and* are emitted over a region where the DEM gradient is small, are overestimated by large factors (up to 10). The DEM_L therefore gives an **incorrect** differential emission measure distribution.

2.5.3 The element abundances evaluation. Comparison of the DEM with the DEM_L method.

With the DEM method the element abundances are found by adjusting their values until the maximum number of lines from different ions follow the same DEM curve. Once one absolute element abundance is fixed, all the other element abundances can be adjusted, aligning the DEM curves of the different elements.This is only possible if there is sufficient temperature overlap for the different elements and the element abundances are assumed not to vary within the observed volume (i.e. not to vary with temperature). **In this case, as in the rest of this thesis, unless otherwise stated, the abundance of oxygen**

has been fixed at the photospheric value $10^{8.93}$ (*Grevesse and Anders*, 1991), and all the other element abundances have been found relative to this. Note that in the recent study of *Grevesse and Sauval* (1998), the oxygen photospheric value has been lowered to $10^{\mathbf{8.83}}$.

For example, for the averaged coronal hole spectrum of *Vernazza and Reeves* (1978), the adopted Ne/O relative element abundance was obtained by deriving a DEM curve from the O III, O IV, O V lines, and requiring an overlap with the DEM curve obtained from the Ne lines (Ne III, Ne IV, Ne V, Ne VI, Ne VII). This resulted in an increase over the photospheric Ne abundance ($10^{8.09}$) of $10^{0.2}$=1.6, while keeping the O abundance equal to the photospheric value. The abundances of Ca and Na were modified in the same way. However, the Ca abundance determination is based on only one line, Ca X 574Å which was blended with a C III line, and so should be treated with caution. The Na abundance was found using two lines, the Na VII (blended) line at 491.9 Å and the bright Na VIII 411.2 Å line.

To have a quantitative idea of the effects of the differences between the adopted and photospheric abundances, theoretical intensities have been calculated for the Ne, Ca, Na lines with the photospheric abundances of *Grevesse and Anders* (1991) and the same DEM, and the results reported in Table 2.2. The ratio $I_{\rm th}/I_{\rm ob}$ clearly shows that these lines are *not* well reproduced. These points are also displayed in Figure 2.13, for a visual confirmation of the need to modify the Ne, Ca, and Na abundances. The same Figure 2.13 also shows the line differential emission measures DEM_L values derived with the photospheric abundances. While nothing can really be said about the blended lines, because of the already mentioned differences between $\rm T_{eff}$ and $\rm T_{max}$, the EM_L values of the O III – Ne III and O IV – Ne IV also show the need to vary the Ne/O abundance. So, both the DEM method and the EM_L method give the same result, in this case. This happens because:

a) such lines have G(T) almost equal (except for a scaling factor) and $T_{\rm eff} = T_{\rm max}$;

b) most of their G(T) is at temperatures where the DEM distribution is relatively flat.

In fact, given two elements X_1 and X_2, the ratio of the observed intensities can be written:

$$\frac{I_1}{I_2} = \frac{A_b(X_1) \int_T C_1(T, N_e)\ DEM(T)\ dT}{A_b(X_2) \int_T C_2(T, N_e)\ DEM(T)\ dT} \tag{2.20}$$

from which the relative element abundance $A_b(X_1)/A_b(X_2)$ can be deduced, from the observed intensity ratio I_1/I_2, once the DEM distribution is known. Only when the two lines have similar $C(T)$ and the DEM distribution is relatively flat would one expect that

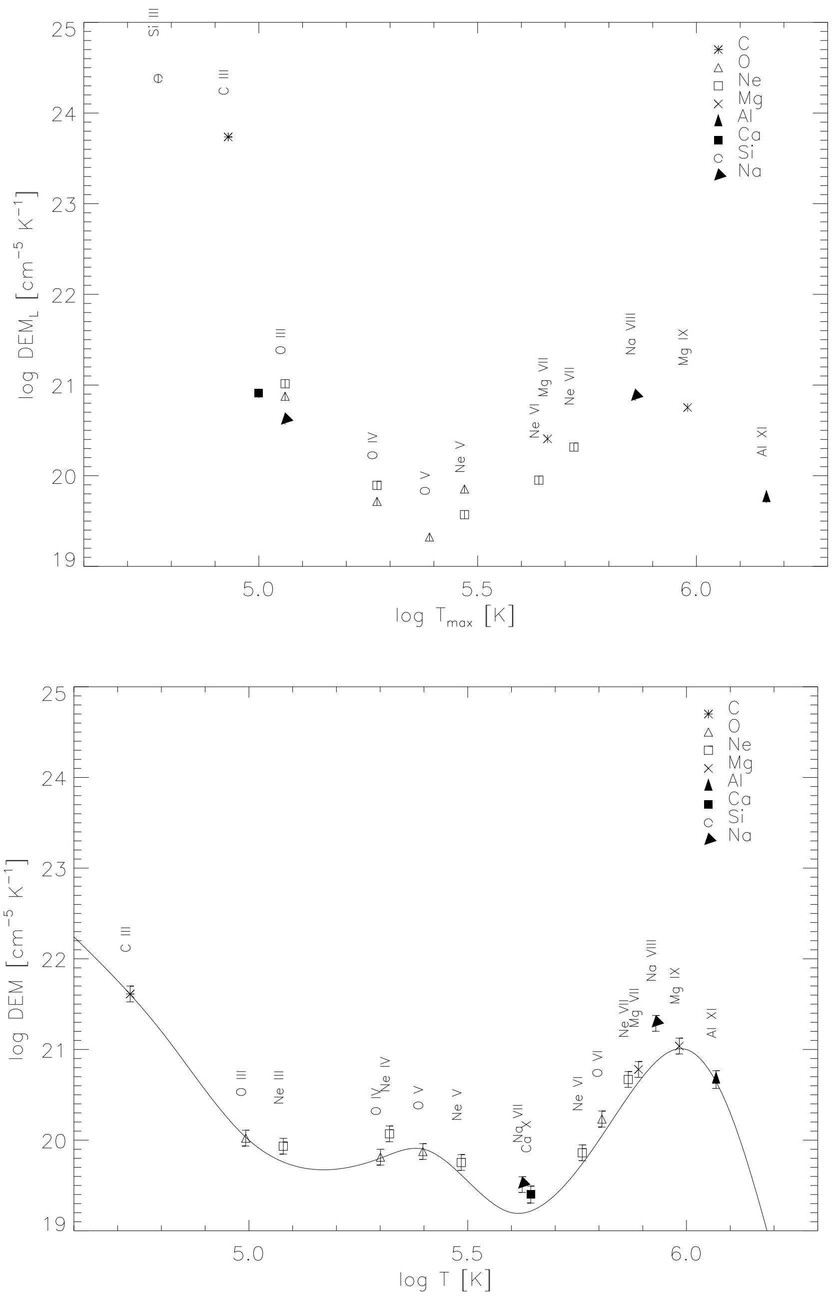

Figure 2.13: *Line differential emission measures DEM_L of the selected lines (top), and DEM with the* Grevesse and Anders *(1991) abundances (bottom), showing the need to modify them for some elements (Ne, Na, and Ca).*

the DEM factors out from the integrals:

$$\frac{\int_T C_1(T,N_e)\ DEM(T)\ dT}{\int_T C_2(T,N_e)\ DEM(T)\ dT} = \frac{\int_T C_1(T,N_e)\ dT}{\int_T C_2(T,N_e)\ dT} \tag{2.21}$$

If the above equality holds, then it is possible to deduce the relative abundances directly from the observed intensities and the contribution functions, because:

$$\frac{A_b(X_1)}{A_b(X_2)} = \frac{I_1 \cdot \int_T C_2(T,N_e)\ dT}{I_2 \cdot \int_T C_2(T,N_e)\ dT} = \frac{DEM_L(X_2)}{DEM_L(X_1)} \tag{2.22}$$

i.e. the DEM method and the DEM_L method are equivalent. In any other case, the two methods can be expected to produce different results. There are many cases in which it is possible to observe lines emitted by ions of different elements that have similar contribution functions $C(T)$, from which relative element abundances have been derived in the past (see Section 2.6 for some examples), assuming the DEM_L method and neglecting what is termed here and in the rest of this thesis 'the DEM effect' on the element abundance derivation. The DEM effect is particularly important when the emissivity $C(T)\ DEM(T)$ of a line peaks at temperatures where there is a non-negligible DEM gradient and Equation 2.21 does not hold. In the averaged coronal hole spectrum of *Vernazza and Reeves* (1978) the DEM distribution is such that the DEM effect can be important at temperatures $logT < 5$ and $logT > 5.6$, but in other spectra the DEM distribution can be very different. The DEM effect becomes particularly important at certain temperatures. In particular, the region $5.5 < logT < 5.8$ is very important for the determination of the FIP effect, because most of the EUV low- and high-FIP lines are emitted in that temperature range, and the DEM effect plays an important role. Section 2.6 discusses this issue and gives some examples.

2.5.4 Discussion of the results and comparison with previous analyses

It is beyond the scope of this chapter to provide a full description of the data analysis and results on the averaged coronal hole spectrum, although interesting. However, before concluding this Section, some general comments on the science rather than the methods are worth noting, in particular because some of the results are relevant in the remainder of this thesis.

First, the DEM method has shown that blending is the major problem when analysing the HCO data. Most of the lines not presented are serious blends, where the principal lines are from different ions and elements. Also, most of the lines at shorter wavelengths could not be well reproduced, which is probably due to intensity calibration errors at wavelengths below 400 Å as also reported by *Warren et al.* (1998), who recently re-analysed the quiet sun data of *Vernazza and Reeves* (1978), performing a DEM analysis. The Mg IX 368 Å line is the strongest line at shorter wavelengths, and has been used in the present work, while it has been rejected by other analyses of the HCO data (*Raymond and Doyle*, 1981b; *Warren et al.*, 1998).

The shape of the DEM and the element abundances

The DEM of the averaged cell-centre coronal hole spectrum is slightly different from that obtained by *Raymond and Doyle* (1981b), reproduced in Figure 2.14. They calculated the EM_T values, integrating the DEM over $logT = 0.1$ intervals, and therefore the comparison should be made with the EM_T values shown in Figure 2.10.

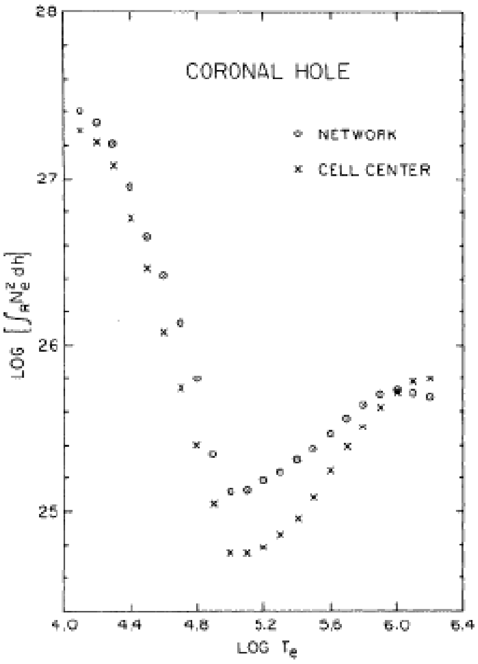

Figure 2.14: *The emission measure distribution (EM_T values) for the coronal hole network and cell centre of* Raymond and Doyle *(1981b), derived from the* Vernazza and Reeves *(1978) data.*

The EM_T values at lower and higher temperatures are basically the same, as is also true for the minimum at $logT = 5.0 - 5.2$. The small increase around $logT = 5.4$ is mainly due to O V lines, while the second minimum around $logT = 5.6$ is mainly required by the Ne V lines. These differences might be due to the improved atomic data used, or to differences in element abundances, while differences in the adopted pressures for the calculation of the contribution functions can be ruled out (although *Raymond and Doyle*

(1981b) do not specify the adopted values). *Raymond and Doyle* (1981b) refer to the previous paper *Raymond and Doyle* (1981a), where contribution functions are calculated with abundances that are close to photospheric. Their adopted log values in their analysis were : He (10.93); C(8.55); N(7.96); O (8.63); Ne(7.60); Mg(7.65); Si(7.65); S(7.20). As well as a departure in the O abundance from the photospheric value (8.93), they took the O/Ne relative abundance to be 10.7. The adopted abundance ratio from the present analysis is $10^{8.93-8.09+0.2}$=4.37, a factor 2.4 lower, which explains part of the difference in the DEM distribution. In any case, it should be noted that *Raymond and Doyle* (1981b) did not use the Ne III, Ne IV, Ne V, Ne VI lines, and their DEM at $logT = 5.0 - 5.6$ K is constrained by O III, O IV, O V, O VI lines. It is therefore not surprising to find differences, because of the different atomic data used, and the line selection and element abundances. This type of difference will be encountered elsewhere in this thesis, and is typical of the state of the art in the field.

The problem with the Li-like ions and other lines

Table 2.4: Some other lines of the averaged coronal hole spectrum of *Vernazza and Reeves* (1978), with the adopted abundances.

Ion	λ_{th} (Å)	λ_{ob} (Å)	Transition	I_{ob}	I_{th}/I_{ob}	+/-	log T_{eff}	log T_{max}	frac
N II	916.011	915.5	2s2 2p2 $^3P_1$ - 2s 2p3 $^3P_2$	18.7	0.89	0.13	4.55	4.73	0.31
N II	915.6		2s2 2p2 $^3P_0$ - 2s 2p3 $^3P_1$					4.73	0.25
N II	916.0		2s2 2p2 $^3P_1$ - 2s 2p3 $^3P_0$					4.73	0.25
N II	916.0		2s2 2p2 $^3P_1$ - 2s 2p3 $^3P_1$					4.73	0.19
O II	718.610	718.0	2s22p3 $^2D_{3/2}$ - 2s2p4 $^2D_{5/2}$	10.6	5.43	0.77	4.65	4.82	0.56
O II	718.5		2s22p3 $^2D_{5/2}$ - 2s2p4 $^2D_{3/2}$					4.82	0.36
N III	991.577	991.4	2s2(^{1}S)2p $^2P_{3/2}$ - 2s 2p2 $^2D_{5/2}$	24.4	0.94	0.13	4.79	4.98	
S IV	1062.661	1062.7	3s2.(^{1}S).3p $^2P_{1/2}$ - 3s.3p2 $^2D_{3/2}$	2.1	0.21	0.03	4.94	5.05	
N IV	765.147	764.3	2s2 $^1S_0$ - 2s 2p $^1P_1$	38.2	0.53	0.07	5.09	5.18	0.69
N III	764.4		2s2 2p $^2P_{3/2}$ - 2s 2p2 $^2S_{1/2}$					5.01	0.20
N III	763.3		2s2 2p $^2P_{1/2}$ - 2s 2p2 $^2S_{1/2}$					5.01	0.11
S VI	933.378	933.1	3s $^2S_{1/2}$ - 3p $^2P_{3/2}$	5.8	0.20	0.03	5.45	5.27	
N V	1238.821	1238.8	1s2 2s $^2S_{1/2}$ - 1s2 2p $^2P_{3/2}$	24.0	0.35	0.05	5.58	5.27	
C IV	419.713	419.5	1s2 2p $^2P_{3/2}$ - 1s2 3s $^2S_{1/2}$	11.2	0.08	0.01	5.74	5.08	0.51
C IV	419.5		1s2 2p $^2P_{1/2}$ - 1s2 3s $^2S_{1/2}$					5.08	0.26
Ca X	419.8		3p $^2P_{3/2}$ - 3d $^2D_{5/2}$					5.82	0.18
Mg X	609.793	609.6	1s2.(^{1}S).2s $^2S_{1/2}$ - 1s2.(^{1}S).2p $^2P_{3/2}$	10.0	5.32	0.75	5.91	6.04	0.73
O IV	609.8		2s2 2p $^2P_{3/2}$ - 2s 2p2 $^2S_{1/2}$					5.27	0.26
Ne VIII	770.409	770.4	1s2 2s $^2S_{1/2}$ - 1s2 2p $^2P_{3/2}$	19.8	6.77	0.96	5.94	5.79	
Mg X	624.941	624.7	1s2.(^{1}S).2s $^2S_{1/2}$ - 1s2.(^{1}S).2p $^2P_{1/2}$	2.4	8.48	1.20	6.02	6.04	

Table 2.4 shows the identifications and results for some other lines in the same spectrum, based on the adopted values of pressure, element abundances, and DEM. The first striking result is the behaviour of the Li-like ions, compared to the others. In fact, N V and C IV are **underestimated**, while Ne VIII and Mg X are **overestimated**, both by large factors. The S VI 933.3 Å (Na-like) is also **underestimated**, but this could be due to an

underestimation of the S abundance. In fact, other S lines (S IV) are also underestimated. No correction was made to the S abundance, because only a few S lines were observed.

Raymond and Doyle (1981b) do not report any such problems, and actually state that '*a good agreement is found between lines of different isoelectronic sequences*', but in reality, to constrain the million-degree peak of the DEM they only used Li-like lines (O VI, Ne VIII, Mg X, Si XII, S XIV), with the exception of Ar VII and Ca X (see Figure 4 of their paper. No comparison with the other sequences was presented by *Raymond and Doyle* (1981b).

Anomalous behaviour of the Li-like ions, together with those of the Na-like isoelectronic sequence, compared to the other sequences, was first discovered by *Dupree* (1972), using OSO-IV quiet sun data (with even lower spectral resolution than ATM), although it has been neglected in most of the subsequent literature on solar EUV spectroscopy, except in a few cases that are mentioned below.

Judge et al. (1995) present a DEM analysis of solar spectra with no spatial resolution (the Sun was observed as a star) and a spectral resolution of 1 Å, based on satellite and rocket data. The spectra were well calibrated, with a photometric accuracy of 15%. With the DEM analysis, *Judge et al.* (1995) found that '*very significant and systematic differences exist between the line intensities of the Li and Na isoelectronic sequences formed below 3* x*10^5 K and those of the other sequences*', and note '*the absence of a discrepancy in the coronal Li-like ions Mg X, Ne VIII*'.

Judge et al. (1995) used the photospheric abundances and performed a DEM analysis on the observed lines of the ions C II, Si III, C II, N III, Si IV, O III, C IV, O IV, N V, O VI, Ne VII, Ne VIII, Mg IX, Mg X, i.e. only a limited number of lines were used. However, considering first the Li-like lines, they found C IV, N V, and O VI lines **underestimated** by factors of 2 to 5.

Although they state no discrepancy for the Ne VIII lines, their $I_{\rm th}/I_{\rm ob}$=1.8, a factor much higher than the stated uncertainties in the calibration as well as the fact that all the other lines are reproduced within 20%. Furthermore, only two lines (Ne VII and Mg IX, Be sequence) were used to constrain the peak of the DEM, and any of their conclusions on the high-temperature lines should be treated with caution. However, considering those two lines, it seems that their DEM is underestimated at higher temperatures. If this underestimation is taken into account, then $I_{\rm th}/I_{\rm ob}$=2.2.

The other Li-like coronal line they used was the bright Mg X 609.8 Å line, for which they state $I_{\rm th}/I_{\rm ob}$=1.07. In reality, this line is a strong blend with an O IV line that is not reported in the paper. If the O IV contribution was indeed neglected, it could easily account for more than 30% of the observed intensity (see Chapter 3 for examples), and with the probable underestimation of the DEM, $I_{\rm th}/I_{\rm ob}$ must be at least 1.7, again an **overestimation** as for the Ne VIII. Regarding the Na sequence, only Si IV was observed, with an **underestimation** by a factor of 2.

In conclusion, the observations presented by *Judge et al.* (1995) are found here to be in agreement with the behaviour of the Li-like ions in this analysis of the coronal hole spectrum, and will be further confirmed in the next Chapter from SOHO/CDS observations. The author agrees on the question posed by *Judge et al.* (1995): '*Why are these results so striking, and yet earlier work failed to identify these systematic effects ?*'; and with the comment that '*the implications are likely to be far-reaching*'. In fact, the probable cause for this effect is a departure from equilibrium, which can be explained with the long timescales of the dielectronic recombination from the He-like ions. If this is true, the large body of work in solar and stellar coronal physics, based on Li-like ions, will have to be revisited.

Recently, *Warren et al.* (1998) also re-analysed the *Vernazza and Reeves* (1978) quiet sun spectral intensities with a DEM method, recent atomic data and coronal abundances. They also found an **underestimate** of the low-temperature Li- and Na-like O VI, N V, S VI lines by factors 2-4. As in *Raymond and Doyle* (1981b), they used the higher temperatures lines of Li- and Na-like ions to determine the $DEM(T)$ around 10^6 K, and therefore no disagreement with the other isoelectronic sequences could be found for those lines. All the other lines were discarded because of the larger uncertainties at the shorter wavelengths. The unfortunate situation in which most of the bright and well-calibrated high-temperature lines observed by the HCO instrument were from Li- and Na-like ions is not repeated in the CDS instrument which does observe high-temperature lines of different isoelectronic sequences. More details on the findings from CDS observations can be found in the following Chapters.

Finally, aside from the Li- and Na-like problems, the examined coronal hole spectrum also showed that many other ions could not be well represented, some of which (such as C II) are emitted at such low temperatures that opacity effects come into play. Another case is O II, which is **overestimated** by a factor of 5. *Warren et al.* (1998) also found an overestimation for the quiet sun data, but only by a factor of 2. The blend N III-N IV at 764 Å is underestimated by a factor of 2. These inconsistencies are found also from CDS spectra, as explained in the following Chapter, which confirms the fact that these findings are not instrument-dependent but are due to incorrect atomic physics or wrong model assumptions.

2.6 The element abundance evaluation. Critical discussion of previous work and assessment of the CDS possibilities

One of the main unresolved issues in the solar corona is the FIP effect and the determination of the coronal abundances. It is therefore important to explain what method was used to derive element abundances, and compare it with the methods that have been previously used.

The ratios of lines emitted by ions of different elements, but having similar contribution functions, were used as proxies for abundance variations, while the differential emission measure analysis was used to deduce relative element abundances (as explained in Section 2.4).

In the past, using Skylab observations, only a limited number of lines could be used unambiguously (due to the characteristics of the overlapping spectroheliograms), and most of the abundance determinations were based on line ratios at the rings of the limb-brightening. The most commonly used ratios were those of Mg VI/Ne VI and Ca IX/Ne VII lines (*Widing and Feldman*, 1989). In particular, most of the abundance determinations found in the literature are based on Mg VI/Ne VI lines, because one is from a low-FIP element (Mg) and the other from a high-FIP element (Ne), and there was much interest in the FIP effect. Although intensity ratios of lines of these ions do show large variations, depending on the structures observed (and presumably on the topology of the magnetic field (*Sheeley*, 1996)), it is not straightforward to deduce from them variations in relative elemental abundances, since various effects can change the observed ratios as well. The most important ones are the DEM effect and the result of density analyses along the line of sight.

Although the possibility of the presence of the DEM effect has been pointed out by some authors, as was the possibility of casting serious doubts on the elemental abundance work (*Phillips*, 1997a), only a few abundance analyses include a full DEM analysis (*Schmelz*, 1993; *Fludra and Schmelz*, 1995; *Del Zanna and Bromage*, 1999a).

The Mg VI contribution functions are slightly skewed toward higher temperatures, compared to the Ne VI ones, as Figure 2.15 shows. The ratio of the contribution functions (also Figure 2.15) shows how the differences increase above temperatures of $10^{5.7}$ K. These kinds of differences are much more pronounced for other pairs of ions, such as Ca IX and Ne VII, or Mg VII and Ne VII, and therefore any effects present in the Mg VI / Ne VI ratios would also be present, and much more important, for these other ions.

The lines emitted by the Mg VI and Ne VI ions have C(T) that peak at temperatures

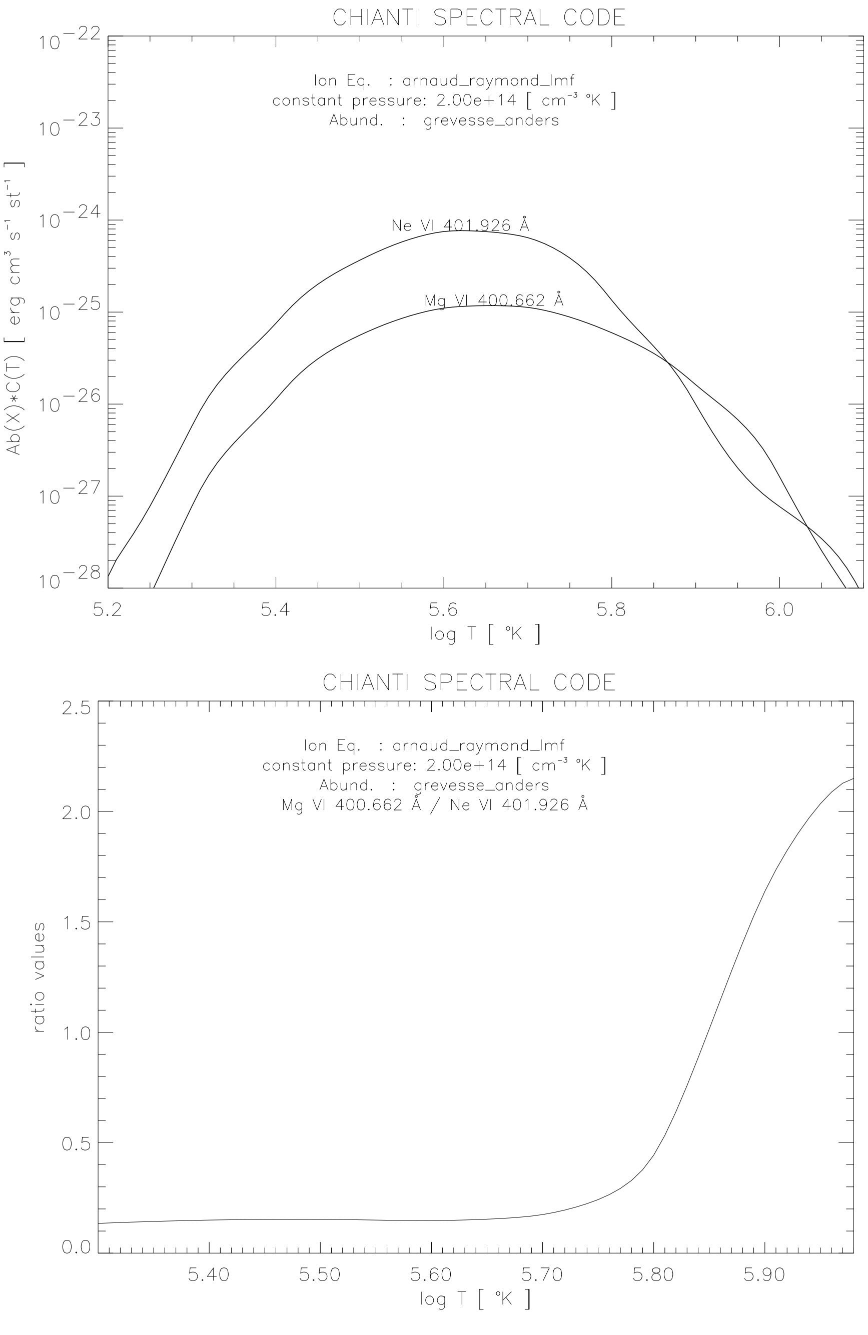

Figure 2.15: *Contribution functions of the two Mg VI 400.666 Å and Ne VI 401.926 Å lines and their ratio, calculated at constant pressure $P_e = 2\ 10^{14}$ [cm^{-3} K], with the ionization equilibrium calculations of* Arnaud and Rothenflug *(1985) and photospheric abundances (*Grevesse and Anders, *1991).*

where the DEM gradient is large in most of the solar observations, and is particularly large for low-temperature structures such as plumes (see Chapter 5). Therefore, these small differences in the contribution functions are amplified when forming the integrals and the relation 2.21 does not hold; the DEM_L method gives the wrong answer. Neglecting the shape of the DEM curves when calculating the Ne/Mg relative abundances using Ne VI and Mg VI ions has the effect of underestimating the Ne/Mg relative abundance, thus overestimating the FIP effect. Any inaccuracy in the ionization equilibrium calculations (or departures from equilibrium) could also be amplified by this DEM effect.

Density variations can also change the observed Mg VI / Ne VI intensity ratios, since most of the Mg VI lines are density-dependent (while the Ne VI are not). In theory, if one can independently measure an electron density pertaining to the region where the Mg VI lines are emitted (in the transition region), then it is possible to accurately calculate the Mg VI emissivities at that density and remove any uncertainty due to density variations. But unfortunately, transition region densities are very difficult to measure, because in the EUV only a few weak density-sensitive lines are observed. The few values previously reported in the literature have a large scatter around typical values of $N_e \simeq 10^9$ cm^{-3} (from Mg VII).

Another source of uncertainty is the fact that when calculating the contribution functions the source region might be better represented with a constant pressure along the line of sight, instead of a constant density. Ideally, if enough density estimates at different temperatures are available, one should calculate the contribution functions $C(T, N_{\rm e})$ with an appropriate density-temperature model, although other effects can still come into play (*Doschek*, 1984). The issue of constant pressure or constant density in the transition region is still an open one, in the sense that there have not been sufficient observational constraints to indicate which is better.

It is useful to see to what extent different densities or pressures can affect the observed ratios. A particular group of Mg VI-Ne VI lines (around 400 Å) has been chosen as an example, because these lines have been widely used in the past (*Sheeley*, 1996), due to the fact that they are close in wavelength and possible calibration errors are much reduced. The line intensities have been calculated at different densities and pressure values, for different DEM distributions, as an exercise to see how these effects change the theoretical ratios.

The group of lines is: Mg VI (399.281, 400.666, 403.31 Å) and Ne VI (399.821, 401.136, 403.255, 401.926 Å). The ratios of these lines, calculated using CHIANTI, compared to the brightest ones in each group (Mg VI 403.31 Å and Ne VI 403.255 Å) are (Mg: 0.35, 0.67, 1.); (Ne: 0.20, 0.38, 0.22, 1.), i.e. the same values that can be deduced from Table 1 in *Widing and Feldman* (1993). These ratios are the same for different densities, because the Ne VI lines are not density-dependent, and the Mg VI lines all have the same density dependence. This confirms the consistency between the atomic data used by other authors in the past (*Widing and Feldman*, 1993) and those used in the present work.

Table 2.5: *Table of theoretical intensity ratios for the Mg VI 400.666 Å /Ne VI 401.926 Å, and Ne VI 401.926 Å /Mg VI (+ Ne VI) 403.3 Å, assuming a relative abundance A_b (Ne/Mg) = 0.5, for a pressure $P_e = 10^{14}$ (cm^{-3} K), different densities N_e (cm^{-3}) and: a) without the consideration of a DEM; b) with a plume DEM (*Del Zanna and Bromage, *1999b); c) with a quiet sun (network) DEM (*Del Zanna and Bromage, *1999a). The values calculated in* Widing and Feldman *for $N_e = 10^{10}$ and those presented by* Sheeley *(1996) are also displayed for comparison in the last two columns.*

	$P_e = 10^{14}$	$N_e = 10^8$	$N_e = 10^{10}$	$N_e = 10^{10}$ *Widing and Feldman* (1993)	*Sheeley* (1996)
			Mg VI 400.666 Å /Ne VI 401.926 Å		
(a)	1.42	1.50	0.90	0.97	1.00
(b)	2.91	3.03	1.76	-	-
(c)	2.18	2.28	1.34	-	-
			Ne VI 401.926 Å /Mg VI (+ Ne VI) 403.3 Å		
(a)	0.43	0.40	0.65	-	0.61
(b)	0.22	0.21	0.36	-	-
(c)	0.29	0.28	0.46	-	-

Two ratios have been selected, from the various possible combinations, the Mg VI 400.666 Å / Ne VI 401.926 Å and Ne VI 401.926 Å / Mg VI (+ Ne VI) 403.3 Å. While the use of the first ratio is preferred, since the lines are unblended, the second is used more in the literature, since the Mg VI 403.31 Å line is the brightest in the group, although blended with Ne VI 403.255 Å. The moderate CDS spectral resolution makes the evaluation of the Mg VI 400.666 Å line difficult, due to the proximity of other lines.

The effects that different *DEM* distributions and different densities have on these two theoretical Mg/Ne intensity ratios were studied, calculating the ratios for a pressure $P_e = 10^{14}$ (cm^{-3} K), typical of coronal holes, and for densities $N_e = 10^8$ and 10^{10} (cm^{-3}), assuming a relative Ne/Mg abundance A_b (Ne/Mg) = 0.5, with different *DEM* distributions. The adopted densities are extreme values, in the sense that previous density estimates of the quiet sun (at the Mg VI temperatures) have produced values within this range. It is therefore to be expected that the possible variations in density affecting the observed ratios are well within the range $N_e = 10^8 - 10^{10}$.

Table 2.5 shows the results. Case (a) is when the *DEM* is neglected in the calculation of the ratio (Equation 2.22). Case (b) is with a plume DEM (*Del Zanna and Bromage*, 1999b), which represents an extreme case, because the steepening of the DEM curve is exactly where the differences between the Mg VI and Ne VI C(T) are maximum, and the DEM effect is greatest. Case (c) is with a more 'normal' quiet sun (network) DEM (*Del Zanna and Bromage*, 1999a). The values calculated in *Widing and Feldman* (1993) for $N_e = 10^{10}$ and those presented by *Sheeley* (1996) are also displayed for comparison.

Table 2.5 shows that the DEM effect is more important than the density effect, and that the values the ratios have with different DEM distributions are quite different from the values stated by *Widing and Feldman* (1993) and *Sheeley* (1996) (and used in all the literature on this topic, for that matter), where no DEM effect was taken into account. It is therefore possible, if not probable, that some of the previous results on elemental abundances, if based on Mg VI/Ne VI lines, produced an underestimate of the Ne/Mg relative abundance of up to a factor of three. Work based on different pairs of lines (e.g. Mg VII/Ne VII) can have produced much larger underestimates.

Some of the published Skylab data, that were used to produce estimates of element abundances, were re-analysed, to see if the DEM effect played a role in those observations. This re-analysis of old Skylab data has shown that in most cases using the full DEM analysis made little difference. Only a couple of examples are briefly discussed here, because they are instructive.

The first is the *Widing and Feldman* (1992) work on off-limb observations of a plume. This is the only work of abundance analysis on plumes ever published. In this work, which focused on the brightest plume observed by Skylab, *Widing and Feldman* (1992) derive a Ne/Mg relative abundance of 0.36, one of the lowest values observed. Although a complete DEM analysis on the same data was not possible, since only a few lines in a restricted temperature range were reported, a limited DEM analysis on those data has indicated that the correct relative Ne/Mg abundance is about a factor of two higher. The DEM and the DEM_L methods are therefore *not* equivalent in this case, as expected, for the reasons explained above. More details on coronal hole plume elemental abundances can be found in Chapters 5 and 6.

The second example is based on the re-analysis of the published data of an erupting prominence observed by Skylab and presented by *Widing et al.* (1986). The contribution functions have been calculated at the same constant density $N_{\mathrm{e}} = 10^{10}$ adopted in their paper. Also the same element abundances, derived in their paper were used, with the only difference that *Widing et al.* (1986) present their results in terms of abundances relative to Mg, while in the present work the abundances are given relative to H, assuming a Mg/H relative abundance of 4x10^{-5}. An estimated 10% error on the published values is reported on the data points. Figure 2.16 shows the comparison of the line emission measures DEM_L and DEM analysis. The DEM in Figure 2.16 shows a peak around the temperatures where the Mg VI and Ne VI lines have maximum emissivities, and therefore at those temperatures the gradient in the DEM is small, and the two methods agree, as one would expect.

The potential of CDS for determining abundances

Unfortunately, all the low temperature lines (log T $\leq$ 5.5 K) observed by CDS/NIS are from high-FIP elements (e.g. N, O, Ne), while all the high temperature lines (log T $\geq$ 5.9 K) are from low-FIP elements (e.g. Mg, Ca, Fe, Si, Al), and the FIP effect is therefore difficult to study. However, considering first these two groups of elements, separately, the number of observed lines and their temperature overlap is good enough to determine quite accurately their relative abundances. For example, the same O III, O IV, O V and Ne III, Ne IV, Ne V lines observed by Skylab are observed by CDS, with a much better resolution, and the O/Ne relative abundance can easily be checked as already shown. Furthermore, these lines are mostly density-insensitive and are observed by the same detector (NIS 2), therefore reducing any calibration problems. The same applies to high-temperature lines, which CDS observes mostly in NIS 1 and the GIS detectors. The number of observed lines is so large that density-insensitive lines can be used, and the determination of the relative abundances is not a problem.

The scaling between high and low-FIP elements can be achieved using low-FIP low-temperature lines and high-FIP high-temperature lines, that overlap in temperature. Unfortunately, NIS observes only a few of these, one Mg VI line at 349.2 Å and three Mg VII lines in NIS 1, and a few Ne VI and Ne VII lines visible in NIS 2. The Mg V lines (NIS 1) are excluded because they are very weak and mostly blended. The determination of the FIP effect is problematic: 1) because there are only a few such lines, and they are visible in different detectors, thus making the relative intensity calibration between NIS 1 and NIS 2 a crucial issue (see Chapter 3 for a complete discussion); 2) these lines fall in the temperature range $logT = 5.6 - 5.8$, where the differential emission measure usually has a steep increase and the shape of the DEM curve affects the abundance determination most, as already explained; and 3) some of these lines are slightly density-sensitive.

The Mg VI line at 349.2 Å is a blend of four Mg VI transitions which are only slightly density-dependent at low densities (their total emissivity varies by 40% in the interval $N_e = 1 \cdot 10^8 - 1 \cdot 10^9$ cm^{-3}). This Mg VI line has the further complication of being blended with a density-dependent coronal line, Fe XI at 349.046 Å . However, the Fe XI contribution can be safely neglected when observing coronal holes and the quiet sun on the disc, and the Mg VI 349.2 Å line can be used in conjunction with the Ne VI 562.8

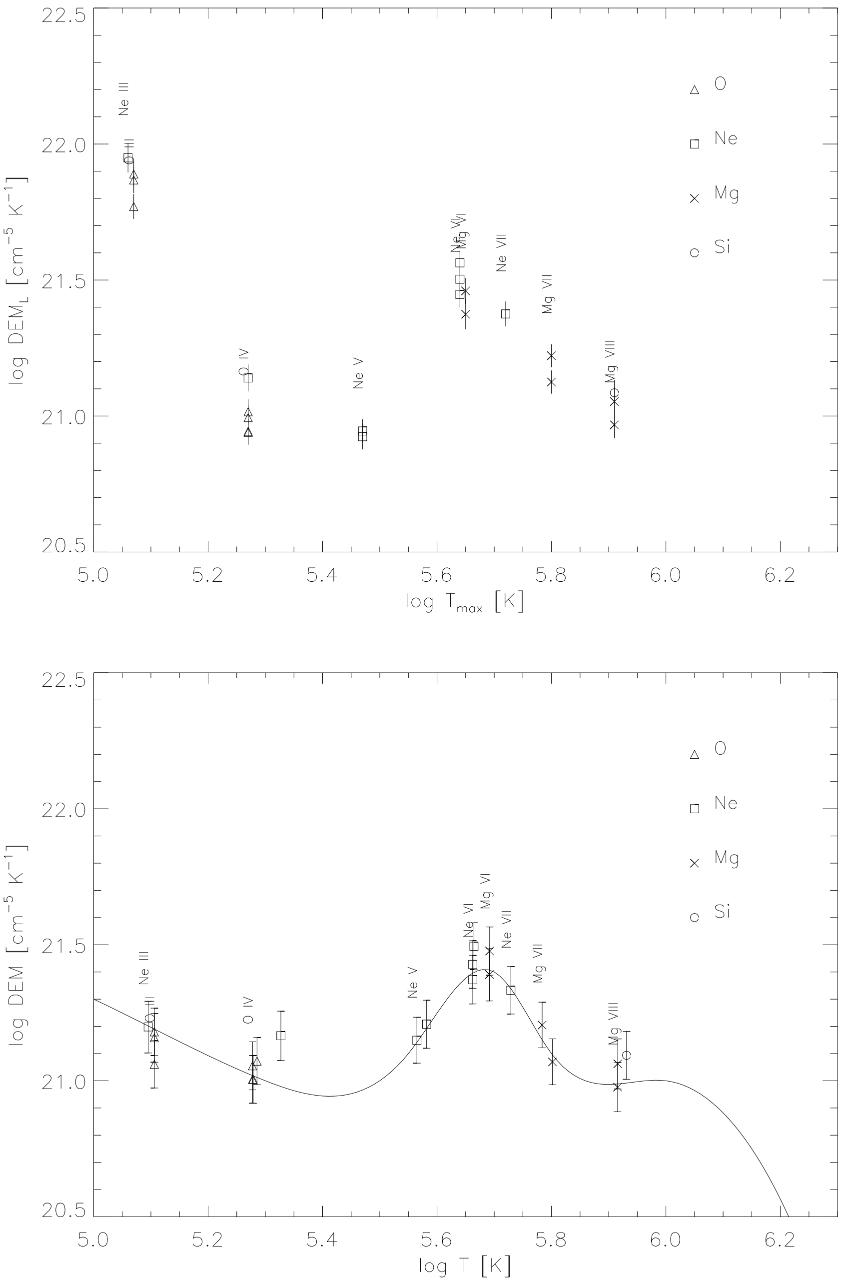

Figure 2.16: *Top: The line differential emission measures DEM_L of the lines of an erupting prominence (*Widing et al.*, 1986), plotted at the temperature $T_{\rm max}$. Bottom: The DEM distribution corresponding to the same lines as above.*

Å when searching for a FIP effect in the solar features observed. The contribution of the Fe XI 349.046 Å line to the observed line can be estimated by combining theory and observations. In fact, at $N_e \simeq 2 \cdot 10^8$ cm^{-3}, the intensity of the Fe XI 349.046 Å line is 1/20 of the intensity of the Fe XI 341.113 Å line, which is observed un-blended. Even in the cell centre regions, where the Mg VI intensity is low, on average the contribution of the Fe XI 349.046 Å line to the blend was found to be less than 5 % for coronal hole observations. In any case, the Fe XI contribution was included in the calculation of the $G(T, N_e)$.

As for the previous example, this Mg VI/ Ne VI ratio is also strongly affected by the DEM effect. For example, assuming the photospheric abundances of *Grevesse and Anders* (1991), a constant pressure of $4 \cdot 10^{14}$ (cm^{-3} K), and a constant DEM distribution, it is found from eqn. 2.20 that the theoretical intensity ratio I[Mg VI 349.17 Å/ Ne VI 562.8 Å] = 0.35. If the contribution functions are folded with a quiet sun DEM distribution for the cell centres (e.g. Figure 6 in *Del Zanna and Bromage*, 1999), the ratio increases to a value of 0.54, while if a coronal hole DEM for the cell centres (same figure) is used the ratio has a value of 0.66. Therefore, small variations in this Mg VI/Ne VI intensity ratio may be due, not just to real changes in the Mg/Ne relative abundance, but also to a change in the DEM distribution.

Given the fact that only a few lines were available for analysis of the FIP effect from CDS/NIS observations, a large effort has been made to perform and analyse CDS/GIS observations to be used in support of the NIS observations, whenever possible. The CDS/GIS observes many useful lines for such an analysis, as for example the group of Mg VI, Ne VI lines around 400 Å previously mentioned, and many other lines of ions that extend the overlapping region between the high-FIP and the low-FIP ions observed (e.g. the Ca IX 466 Å and Ne VII 465 Å lines). The use of different ions from different isoelectronic sequences is very important because it can help to indicate where the atomic physics may be in disagreement with the observations.

Unfortunately, the analysis of GIS spectra is very complex, for example some of the useful lines can be affected by *ghosts* or second order lines. The use of GIS lines for abundance analysis therefore strongly depends on an assessment of the performance of the GIS detectors, which will be described in the next Chapter.